eNeuro Accepted Manuscript

eNeuro

Research Article: INew Research | Neuronal Excitability

Cell-Type Specificity of Neuronal Excitability and Morphology in the Central Amygdala

https://doi.org/10.1523/ENEURO.0402-20.2020

Cite as: eNeuro 2020; 10.1523/ENEURO.0402-20.2020

Received: 18 September 2020
Accepted: 12 October 2020

This Early Release article has been peer-reviewed and accepted, but has not been through the composition and copyediting processes. The final version may differ slightly in style or formatting and will contain links to any extended data.

Alerts: Sign up at www.eneuro.org/alerts to receive customized email alerts when the fully formatted version of this article is published.

Copyright © 2020 Adke et al.
This is an open-access article distributed under the terms of the Creative Commons Attribution 4.0 International license, which permits unrestricted use, distribution and reproduction in any medium provided that the original work is properly attributed.

eNeuro Accepted Manuscript

1. **Manuscript title:** Cell-type specificity of neuronal excitability and morphology in the central amygdala
2. **Abbreviated title:** Electrophysiological and morphological properties of CeA neurons
3. **Authors and Affiliations:** Anisha P. Adke[1], Aleisha Khan[1]*, Hye-Sook Ahn[1]*, Jordan J. Becker[1], Torri D. Wilson[1], Spring Valdivia[1], Yae K. Sugimura[1], Santiago Martinez Gonzalez[1] and Yarimar Carrasquillo[1#]
[1]National Center of Complementary and Integrative Health, National Institutes of Health, Bethesda, MD, United States.
*These authors contributed equally to this work
4. **Authors Contributions:** Y.C., A.P.A. and S.V. designed research; A.P.A., A. K., H.-S.A., J. J. B., T.D.W., S.V., Y. K. S, and S. M. G performed research; A.P.A., A. K., H.-S.A., Y.K.S, and S.V. analyzed data; A.P.A and Y.C. wrote the paper.
5. **Correspondence:**
Yarimar Carrasquillo, PhD
National Center for Complementary and Integrative Health
National Institutes of Health
35 Convent Drive
Building 35A / Room 1E-410
Bethesda, MD 20892
Phone: 301-451-8147
Fax: 301-480-0772
Email: yarimar.carrasquillo@nih.gov
6. **Number of Figures:** 12
7. **Number of Tables:** 3
8. **Number of Multimedia:** 2
9. **Number of words in Abstract:** 157
10. **Number of words for Significance Statement:** 125
11. **Number of words for Introduction:** 584
12. **Number of words for Discussion:** 2196
13. **Acknowledgements:** We would like to thank Drs. Hugo Tejeda, Mario Penzo and Yavin Shaham for comments on this manuscript and Dr. Ted Usdin and the Systems Neuroscience Imaging Resource of the National Institute of Mental Health

for making possible the morphological reconstruction and analysis of biocytin-filled cells. We would also like to thank the National Institutes of Neurological Disorder Mouse Facility staff for their vital work in animal husbandry.

14. **Conflict of Interest:** Authors report no conflict of interest.
15. **Funding sources:** This research was supported by the National Center for Complementary and Integrative Health Intramural Research Program.

eNeuro Accepted Manuscript

eNeuro Accepted Manuscript

ABSTRACT

Central amygdala (CeA) neurons expressing protein kinase C delta (PKCδ$^+$) or Somatostatin (Som$^+$) differentially modulate diverse behaviors. The underlying features supporting cell-type-specific function in the CeA, however, remain unknown. Using whole-cell patch-clamp electrophysiology in acute mouse brain slices and biocytin-based neuronal reconstructions, we demonstrate that neuronal morphology and relative excitability are two distinguishing features between Som$^+$ and PKCδ$^+$ neurons in the laterocapsular subdivision of the CeA (CeLC). Som$^+$ neurons, for example, are more excitable, compact and with more complex dendritic arborizations than PKCδ$^+$ neurons. Cell size, intrinsic membrane properties, and anatomical localization were further shown to correlate with cell-type-specific differences in excitability. Lastly, in the context of neuropathic pain, we show a shift in the excitability equilibrium between PKCδ$^+$ and Som$^+$ neurons, suggesting that imbalances in the relative output of these cells underlie maladaptive changes in behaviors. Together, our results identify fundamentally important distinguishing features of PKCδ$^+$ and Som$^+$ cells that support cell-type-specific function in the CeA.

Keywords: central amygdala, Somatostatin, protein kinase C delta, intrinsic excitability, morphology, neuropathic pain

SIGNIFICANCE STATEMENT

Genetically distinct neurons in the central nucleus of the amygdala (CeA) are functionally opposed in the modulation of many behavioral outputs, including fear and pain-related behaviors. In this study, we use whole-cell patch-clamp electrophysiology in acute mouse brain slices in combination with molecular genetics and biocytin-based neuronal reconstructions to characterize protein kinase C delta-expressing (PKCδ$^+$) and somatostatin-expressing (Som$^+$) neurons in the CeA. Our experiments revealed striking differences in both electrophysiological and morphological properties of these two subpopulations of

eNeuro Accepted Manuscript

CeA neurons–Som$^+$ neurons are more excitable, compact, and have more complex dendritic arborizations compared to PKCδ$^+$ neurons. These results support the notion that genetically distinct CeA neurons have differing functions and properties, advancing our understanding of the mechanisms underlying cellular and functional heterogeneity in the CeA.

INTRODUCTION

The laterocapsular subdivision of the central nucleus of the amygdala (CeLC) has received increasing interest due to its widespread function in mediating innate, as well as learned, adaptive and maladaptive behaviors. Previous work has demonstrated, for example, that the CeLC is functionally diverse, modulating fear conditioning and aversion (Aggleton, 2000; Davis & Whalen, 2001), nociception (Zald, 2003; Neugebauer *et al.*, 2004; Veinante *et al.*, 2013), anxiety, and drug reward and relapse in rodent models (Gilpin *et al.*, 2015; Venniro *et al.*, 2017; Venniro *et al.*, 2018), to name a few. This diverse span of function is mirrored by the genetic, physiological and morphological heterogeneity in central amygdala (CeA) neuron subtypes (Martina *et al.*, 1999; Schiess *et al.*, 1999; Janak & Tye, 2015).

Two genetically identified cell types, protein kinase C delta-expressing (PKCδ$^+$) neurons and somatostatin-expressing (Som$^+$) neurons, constitute most CeLC neurons and are largely non-overlapping (Li *et al.*, 2013; Kim *et al.*, 2017; Wilson *et al.*, 2019). PKCδ$^+$ and Som$^+$ neurons in the CeA undergo differential plasticity in the context of behavioral output and they both have critical, but distinct, functions in the modulation of CeA-dependent behaviors, including fear conditioning and pain-related behaviors. The activity of PKCδ$^+$ cells, for example, is reduced following exposure to a conditioned stimulus after fear conditioning (Haubensak *et al.*, 2010) but increased following nerve injury (Wilson *et al.*, 2019). In contrast, Som$^+$ cells respond to a threat stimulus by increasing their activity (Yu *et al.*, 2016) but their excitability is decreased following nerve injury (Wilson *et al.*, 2019). Consistent with these correlational changes in excitability, both Som$^+$ and

eNeuro Accepted Manuscript

PKCδ$^+$ CeA neurons have been shown to differentially contribute to fear and pain-related behaviors (Haubensak *et al.*, 2010; Li *et al.*, 2013; Yu *et al.*, 2016; Wilson *et al.*, 2019). The underlying features that support cell-type-specific opposite functions of these genetically distinct CeA neurons, however, remain unclear.

Previous studies have demonstrated that the electrophysiological and morphological properties of CeLC neurons are highly heterogeneous across different species (Schiess *et al.*, 1999; Dumont *et al.*, 2002; Chieng *et al.*, 2006; Li & Sheets, 2018). Recent studies have further shown that CeLC neurons with different firing properties are topographically organized based on their projection targets (Li & Sheets, 2018), suggesting that heterogeneity of function within the CeLC might also be anatomically defined.

In the present study, we contributed to the growing body of knowledge about the CeLC by performing a characterization of the electrophysiological and morphological properties of PKCδ$^+$ and Som$^+$ neurons. Our overarching hypothesis is that these two genetically distinct populations of CeLC neurons are electrophysiologically and morphologically different. We used whole-cell patch-clamp electrophysiology in acute mouse brain slices in combination with biocytin-based morphological reconstructions to characterize and compare the passive and active membrane properties, as well as the evoked repetitive firing responses, single action potential waveforms and neuronal morphologies of these two subpopulations of neurons. We further evaluated whether membrane properties and excitability are dependent on the anatomical localization within the central amygdala, both at the subnuclei and rostro-caudal levels.

Finally, using a mouse model of neuropathic pain, we tested whether perturbations known to alter CeLC-dependent behavioral outputs would result in a shift in the relative excitability of these two CeLC cell types. Using this cell-type-specific approach, we demonstrated that PKCδ$^+$ and Som$^+$ neurons have distinct electrophysiological and morphological properties and that the differences in the excitability of these cells are occluded in the context of neuropathic pain. Our

eNeuro Accepted Manuscript

combined findings provide an essential foundation for understanding functional heterogeneity within the CeA.

eNeuro Accepted Manuscript

MATERIALS AND METHODS

Subjects

All animal procedures were performed in accordance with the guidelines of the National Institutes of Health (NIH) and were approved by the Animal Care and Use Committee of the National Institute of Neurological Disorders and Stroke and the National Institute of Deafness and other Communication Disorders. Adult (9- to 17-weeks-old) male mice were used for all experiments. *Prkcd*-cre heterozygote male or female mice (GENSAT-founder line 011559-UCD) were obtained from the Mutant Mouse Resource and Research Center (MMRRC) at University of California at Davis, an NIH-funded strain repository. This line was donated to the MMRRC by Drs. Nathaniel Heintz and Charles Gerfen (Gong *et al.*, 2003; Gong *et al.*, 2007). *Sst*-cre heterozygote males (Jackson Laboratory – founder line 018973) were obtained from the Jackson Laboratory and donated by Dr. Z. Josh Huang (Taniguchi *et al.*, 2011; He *et al.*, 2012). *Prkcd*-cre and *Sst*-cre mice were crossed with homozygous Ai9 (Jackson Laboratory – founder line 007909) mice. The fidelity and penetrance of Cre in PKCδ^{+} or Som^{+} neurons in the CeA has been previously characterized in these mouse lines (Taniguchi *et al.*, 2011; Wilson *et al.*, 2019). Offspring mice were genotyped for the presence of cre-recombinase using DNA extracted from tail biopsies and PCR (Transnetyx) with the following primers: TTAATCCATATTGGCAGAACGAAAACG (forward) and CAGGCTAAGTGCCTTCTCTACA (reverse). Mice were housed in single cages or in pairs with littermates, separated by a perforated Plexiglass divider and kept in a reversed 12-hour light/dark cycle, with lights on from 9 pm to 9 am. Food and water were provided *ad libitum*. Prior to all experiments, mice were handled as previously described for at least 5 days to minimize potential stress effects associated with handling (Hurst & West, 2010). While handling, mice were also administered a 0.1 mL saline intraperitoneally by the same experimenter that would be anesthetizing it for perfusion and acute slice preparation.

Ex-vivo electrophysiology

eNeuro Accepted Manuscript

Acute slice preparation - Mice were deeply anesthetized using 1.25% Avertin (0.4 mg/g body weight) injected intraperitoneally and then transcardially perfused with ice-cold cutting solution composed of (in mM) 110 choline chloride, 25 $NaHCO_3$, 1.25 NaH_2PO_4, 2.5 KCl, 0.5 $CaCl_2$, 7.2 $MgCl_2$, 25 D-glucose, 12.7 L-ascorbic acid, and 3.1 pyruvic acid, oxygenated with 95%/5% O_2/CO_2. The brains were rapidly extracted, placed in ice-cold cutting solution, and cut in coronal slices (250 - 300 µm) using a Leica VT1200 S vibrating blade microtome (Leica Microsystems Inc., Buffalo Grove, IL, USA). Slices containing the CeA were incubated at 33ºC for 30 minutes in a holding chamber containing artificial cerebral spinal fluid (ACSF) composed of (in mM) 125 NaCl, 2.5 KCl, 1.25 NaH_2PO_4, 25 $NaHCO_3$, 2 $CaCl_2$, 1 $MgCl_2$, and 25 D-glucose. The chambers containing the slices were then moved to room temperature, and slices recovered for at least 20 minutes prior to recording. During incubation and recovery, the chambers were continuously oxygenated with 95%/5% O_2/CO_2. Experiments were replicated with 17 *Prkcd*-cre and 10 *Sst*-cre male mice.

Whole-cell patch-clamp recordings - The recording chamber was perfused continuously with ACSF oxygenated with 95%/5% O_2/CO_2 (1 mL/min) and all recordings were performed at 33±1ºC. A recording chamber heater and an in-line solution heater (Warner Instruments) were used to control and monitor the bath temperature throughout the experiment. Recording pipettes (3-5 MΩ resistance) were filled with internal solution composed of (in mM) 120 potassium methyl sulfate, 20 KCl, 10 HEPES, 0.2 EGTA, 8 $NaCl_2$, 4 Mg-ATP, 0.3 Tris-GTP, and 14 phosphocreatine with a pH of 7.3 using 5 M KOH and an osmolarity of ~300 $mosmol^{-1}$. Biocytin (3 mg/mL) was added to the internal solution of some recordings and sonicated in ice-cold water for 20 minutes. Whole-cell current-clamp recordings were obtained from tdTomato-expressing CeLC neurons in the right hemisphere. Cells were visually identified using an upright microscope (Nikon Eclipse FN1) equipped with differential interference contrast optics with infrared illumination and epifluorescence. Recording electrodes were visually positioned in the CeLC, guided by the distinctive fiber bundles and anatomical landmarks

eNeuro Accepted Manuscript

delineating its structure (**Figure 1B**). Recordings were controlled using the Multiclamp 700B patch-clamp amplifier interfaced with a Digidata 1500 acquisition system and pCLAMP 10.7 software (Axon Instruments, Union City, CA) on a Dell computer. Before forming a membrane-pipette seal, pipette tip potentials were zeroed and pipette capacitances and series resistances (not exceeding 20 MΩ) were monitored throughout the recordings. Whole-cell capacitance was measured in voltage-clamp configuration, with the cell held at -70 mV then subjected to a 25 ms ±10 mV current change. Spontaneously active cells were recorded gap-free in current-clamp configuration for 10 seconds. Brief (5 ms) and prolonged (500 ms) depolarizing current of various amplitudes were injected from resting membrane potential to cells that were silent at rest, to elicit single and repetitive action potential firing, respectively. Liquid junction potentials were not corrected during recordings. All recordings were acquired at 100 kHz and filtered at 10 kHz.

Data Analysis – The sample sizes used in each experiment were based on the standards set forth by the field. At least ten mice were used as biological replicates for all electrophysiology experiments, rather than repeating identical tests on a single sample to generate technical replicates. Cells were allocated into experimental groups based on genotype (PKCδ^{+} or Som^{+}). Electrophysiological data were analyzed using ClampFit 10.7 (Molecular Devices), Microsoft Excel, Mini Analysis (v. 6.0.7, Synaptosoft, Inc., Decatur, GA), and Prism (v. 8, GraphPad Software Inc., La Jolla, CA). Data obtained from naïve animals and animals that received a sciatic nerve sham surgery were pooled and used to analyze baseline properties as no significant differences were seen between these conditions.

Single action potential properties were measured from the action potentials generated in response to a 5 ms depolarizing current injection. Current threshold for action potential generation ($I_{threshold}$) was defined as the minimum current injection required to elicit an action potential. Voltage threshold ($V_{threshold}$) was calculated from the third derivative of the variation in membrane potential as a function of time during the rise of the action potential using the Mini Analysis

eNeuro Accepted Manuscript

software. Differentiated traces were digitally Gaussian filtered and smoothed by 30-100 points. Action potential duration (APD) was measured at 100% repolarization to voltage threshold ($V_{threshold}$). Rise time was defined as the time required for the membrane potential to reach peak voltage from $V_{threshold}$ and decay was defined as the time required for the membrane potential to repolarize from 90% of its peak to $V_{threshold}$. Phase plots of single action potentials were generated by plotting the first derivative of the variation in membrane potential as a function of the membrane potential. Action potential afterhyperpolarization (AHP) was calculated from the phase plots of single action potentials and was defined as the voltage at which the first derivative of the variation in membrane potential during the repolarizing phase of the action potential reached zero or switched polarity.

Input resistance (R_{in}) was calculated using the average change in membrane potential in response to a ±20 pA current injection of 500 ms duration. Rheobase was defined as the minimum current required to induce an action potential in response to a 500 ms depolarizing current injection for both late-firing and regular-spiking neurons. Latency to fire for PKCδ$^+$ vs Som$^+$ cells comparisons was calculated at 2x rheobase and was defined as the time between current injection onset to action potential threshold. Voltage sag was calculated from the difference between the steady state and peak voltage responses to a 500 ms 500 pA hyperpolarizing current injection. Accommodation of inter-spike interval (ISI), action potential amplitude, action potential duration (calculated at 50% repolarization relative to voltage threshold) and afterhyperpolarization amplitude were calculated from the ratio of the measurements obtained from the last and first action potential in response to a 500 ms depolarizing current injection at 2x rheobase. ISI accommodating cells were defined as cells with a ratio greater than or equal to 1.5 whereas ISI non-accommodating cells had a ratio of less than 1.5.

Latency to first spike was used to classify cells as late-firing or regular-spiking neurons. Cells with latencies shorter than 100 ms (at baseline) or 90 ms (pain conditions) were classified as regular-spiking. Conversely, cells with latencies

eNeuro Accepted Manuscript

higher than 100 ms (at baseline) or 90 ms (pain conditions) were classified as late-firing. Current amplitudes that elicited an average of 10 spikes (range of 5-19 spikes) were used to calculate latencies to first spike and, subsequently, to classify cells as late-firing or regular-spiking. In baseline (no pain) conditions, this current amplitude was 220 pA for Som^+ cells and 280 pA for $PKC\delta^+$ neurons. Current amplitudes of 220 pA were used for both Som^+ and $PKC\delta^+$ neurons in pain conditions. Number of spikes in response to a 500 ms depolarizing current injection of 140 pA (regular-spiking cells) or 240 pA (late-firing cells) amplitude was used to evaluate subnuclei and rostro-caudal differences in firing responses as well as firing responses as a function of whole-cell capacitance. Whole-cell membrane capacitance was calculated by integrating the capacitive transients elicited by a 25 ms voltage step (±10 mV) from -70 mV.

Spontaneously active neurons were analyzed by selecting a 5 second segment of stable firing. Firing frequency was calculated as the number of action potentials fired divided by 5 seconds. Interspike (IS) potential was calculated as the average membrane potential between two spikes, when the membrane potential plateaus and is stable, after the AHP of one spike and before voltage threshold of the next spike. Peak voltage was measured as the most depolarized potential reached during an action potential. Capacitance, R_{in}, $V_{threshold}$, rise, decay, APD, and AHP of spontaneously active cells were calculated using the methods described above. Single action potential parameters (IS potential, peak voltage, $V_{threshold}$, rise, decay, APD, and AHP) were calculated for each action potential within the 5 second selected trace and averaged, for a single value per cell. Analysis was performed blind to cell genotype. Recording sites were constructed using the Mouse Brain Atlas as a guide (Paxinos *et al.*, 2001).

Morphological reconstruction of biocytin-filled cells

Preservation and staining of biocytin-filled neurons - Following current-clamp recordings, we followed procedures previously described to remove the recording electrode from the cell and retain the morphology of the cell (Swietek *et al.*, 2016).

eNeuro Accepted Manuscript

In brief, the recording pipette was moved in slow alternating steps upward and outward in voltage-clamp mode while continuously monitoring the capacitive transients in order to reestablish a seal. Following re-sealing, the slice was left in the recording chamber for approximately three minutes to ensure transport of biocytin to distal processes. The slice was then removed from the recording chamber and immediately placed into 4% paraformaldehyde solution in 0.1 M Phosphate Buffer (PFA/PB), pH 7.4, at 4ºC for 48 hours, followed by 0.1 M Phosphate Buffered Saline (PBS) (pH 7.4) with 0.01% sodium azide at 4ºC until staining. Slices were rinsed with 0.1 M PBS 3 times for 5 minutes at room temperature while shaking at a low speed, then incubated in PBS containing 0.1% Triton-X-100 for 10 minutes. Samples were then incubated overnight, at 4ºC and protected from light, in 1:500 Alexa Fluor 647 Streptavidin (Jackson 016-600-084) in blocking solution containing 1.5% normal goat serum (NGS) (Vector Labs, Burlingame, CA), 0.1% Triton-X-100, 0.05% Tween-20, and 1% bovine serum albumin (BSA). In minimal light, slices were then washed in 0.1 M PBS 4 times for 30 minutes at room temperature. Slices were then cleared using increasing concentrations of 2,2'-thiodiethanol (TDE) for 10 minutes each using 10, 30, 60, and 80% concentrations (Costantini *et al.*, 2015), followed by incubation in 97% TDE for two hours. Slices were then mounted on positively-charged glass slides and covered with glass coverslips using 97% TDE.

Image acquisition, three-dimensional morphological reconstruction and analysis - Images of recovered biocytin-filled neurons were taken using a Nikon A1R laser scanning confocal microscope with a 40x oil-immersion objective. Gain and pinhole size were kept constant between experiments. Sequential acquisition of z-stacks was collected at 0.09 µm steps. Images were collected at varying sizes, depending on the extension of the dendrites of each neuron, and were then automatically stitched upon acquisition using NIS Elements software. To quantify neuronal morphology, z-stacks were analyzed using Neurolucida 360 (NeuroLucida 360, MBF Bioscience, Williston, VT). Cell bodies were identified using automatic detection of a user-defined area and dendritic branches were traced using the

eNeuro Accepted Manuscript

user-guided tree-tracing function. To identify spines, automatic spine detection was performed using image noise filtering. The experimenter manually confirmed or rejected all parameters analyzed. Primary dendrites were defined as the dendrites directly extending from the soma. Secondary dendrites branched from primary dendrites, and tertiary dendrites were the branching points of secondary dendrites. Dendritic length was defined as the distance from the trunk of the branch to either the distal branching point, or the visible end of the projection. Spine density was calculated by counting the individual spines present on the dendrites and reported per 100 µm of dendrite. Dendritic properties were obtained using branched-structure and Sholl analysis functions from NeuroLucida Explorer. The number of dendritic intersections at increasing radial distances from the soma, in 10 µm increments, were quantified and used for the Sholl analysis. Immunohistochemistry, image acquisition, and morphological reconstruction was performed with the experimenter blind to cell-type.

Immunohistochemistry

Sst-cre::Ai9 mice were deeply anesthetized with 1.25% Avertin (2,2,2-tribromoethanol and tert-amyl alcohol in 0.9% NaCl; 0.025 ml/g body weight) and were then perfused transcardially with 37°C 0.9% NaCl, followed by 100 mL of ice-cold 4% PFA/PB. The brains were carefully dissected and post-fixed overnight in 4% PFA/PB at 4°C. After cryoprotection in 30% sucrose/PB for 48 h, the brains were sliced in 30 µm coronal sections using a freezing sliding microtome. The sections were stored in 0.1 M Phosphate Buffered Saline (PBS), pH 7.4 containing 0.01% sodium azide (Sigma) at 4°C until immunostaining. To begin staining, sections were rinsed in PBS, then incubated in PBS containing 0.1% Triton X100 for 10 minutes at room temperature, followed by blocking at room temperature for 30 minutes in blocking solution containing 5% normal goat serum (NGS) (Vector Labs, Burlingame, CA), 0.1% Triton X100, 0.05% Tween-20 and 1% bovine serum albumin (BSA). Sections were then incubated for 72 h at 4°C in mouse anti-PKCδ primary antibody (1:1000, BD Biosciences, 610397) in blocking solution containing

eNeuro Accepted Manuscript

1.5% NGS, 0.1% Triton X100, 0.05% Tween-20 and 1% BSA. Following the primary antibody incubation, sections were rinsed in PBS and incubated in Alexa Fluor 647-conjugated goat anti-mouse (1:100, Invitrogen, A21235) secondary antibody in blocking solution containing 1.5% NGS, 0.1% Triton X100, 0.05% Tween 20 and 1% BSA for 2 hours at room temperature and protected from light. Sections were rinsed in PBS, mounted on positively charged glass slides, and left overnight to air-dry before coverslips were set using Fluoromount-G (SouthernBiotech). Representative high magnification images were collected using a Nikon A1R laser scanning confocal microscope and a 40x oil-immersion objective. Laser intensity, gain, and pinhole were kept constant between images. Sequential acquisition of multiple channels was used, and z-stacks were collected at 0.9 µm steps. Images were collected at a size of 0.7 x 0.59 mm and were automatically stitched upon acquisition using NIS Elements software. Image stacks were converted into maximum intensity z-projections using the NIS Elements software. Anatomical limits of each region were identified using a mouse brain atlas (Franklin & Paxinos, 2008).

Sciatic nerve surgeries and nociceptive testing

Sciatic cuff implantation - Sciatic nerve cuff and sham surgeries were performed as previously described (Benbouzid *et al.*, 2008). In brief, 13 male *Prkcd*-cre and 10 male *Sst*-cre mice were anesthetized using 2% isoflurane (0.5 L/min). A 1-cm long incision was made along the proximal third of the lateral left thigh and the sciatic nerve was exteriorized and gently stretched using forceps. The nerve was either returned to its normal position (sham animals) or a 2 mm piece of PE-20 non-toxic, sterile polyethylene tubing (0.38 mm ID/1.09 mm OD) was split along and slid onto the sciatic nerve (cuff animals). After returning the nerve to its normal position, wound clips were used to close the skin. All electrophysiological and behavioral experiments were performed 6-14 days following surgeries.

Nociceptive testing - Mice were habituated to the 11 × 11 × 13 cm ventilated Plexiglas testing chambers placed on an elevated mesh platform (for von Frey and

eNeuro Accepted Manuscript

366 acetone tests) or a clear glass surface heated to 30°C (for Hargreaves test) for 1-3
367 h prior to testing. von Frey filaments (North Coast Medical, Inc. San Jose, CA)
368 were used to assess mechanical sensitivity as previously described (Carrasquillo &
369 Gereau IV, 2007). Beginning with the smallest fiber, the experimenter applied
370 filaments to the hind-paw until the filament bent ~ 30° for ~2 s. The smallest
371 filament to evoke a paw withdrawal response in at least three of five trials was
372 recorded as the paw withdrawal threshold. Thermal sensitivity to heat was
373 assessed using a modified version of the Hargreaves test (Hargreaves *et al.*, 1988)
374 as described previously (Carrasquillo & Gereau IV, 2007). A thermal stimulus with
375 an active intensity of 35 was delivered from a constant radiant heat source through
376 the glass bottom of the chamber to the plantar surface of the hind-paw (IITC Life
377 Sciences, Woodland Hills, CA) and the latency to elicit paw withdrawal was
378 recorded. To measure sensitivity to cold, we adapted the acetone evaporative test
379 (Choi *et al.*, 1994). Acetone (Sigma) was drawn into a 1 mL syringe and a drop
380 was lightly applied to the hind-paw through the wire mesh. The drop of acetone
381 (and not the syringe tip) was placed against the plantar surface of the hind-paw.
382 Nociceptive responses and pain-like behaviors were quantified for 60 s following
383 acetone exposure. Response quantification was modeled after a previously
384 reported scoring system (Colburn *et al.*, 2007). Transient lifting, licking, or shaking
385 of the hind-paw that subsided immediately was given a score of 0; the same
386 behaviors continuing up to but not past 5 s after initial application was given a
387 score of 1; repeated and prolonged lifting, licking, or shaking of the hind-paw was
388 given a score of 2. Three to five measurements were taken for each hind-paw on
389 each behavioral assay and the average paw withdrawal thresholds (von Frey), paw
390 withdrawal latencies (Hargreaves) and nociceptive scores (acetone) were
391 calculated individually for each hindpaw. Hypersensitivity was assessed by
392 comparing withdrawal thresholds in the paw ipsilateral to the side of sciatic nerve
393 surgery compared to the paw contralateral to the side of sciatic nerve surgery. For
394 all nociceptive tests, the experimenter was blind to whether the mouse had
395 received cuff implantation or a sham surgery.

eNeuro Accepted Manuscript

396 **Statistics**

397 Results are expressed as mean ± standard errors of the mean (SEM). Outliers
398 were identified as values over two standard deviations above or below the mean of
399 the sample and were subsequently excluded from analyses. Analysis was
400 performed using either Student's unpaired t-tests (with or without Welch's
401 correction for variance), Mann-Whitney U tests, Chi-squared (one-sided) tests, or
402 two-way analyses of variance (ANOVA) followed by posthoc Tukey, Sidak's or
403 Dunnett's multiple comparison tests. The appropriate statistical test was
404 determined after assessing each dataset's normality and variance. All analyses
405 were performed using GraphPad Prism (v. 8) and *p* values lower than 0.05 were
406 considered significant and are reported in figure legends. Detailed information for
407 all statistical tests performed are reported in **Table 3**.

408 **Data availability**

409 All data in this study is available from the corresponding author.

410

eNeuro Accepted Manuscript

RESULTS

Som$^+$ cells are more excitable than PKCδ$^+$ neurons

Previous studies have shown cell-type-specific alterations in the firing responses of PKCδ$^+$ and Som$^+$ neurons following fear conditioning or nerve injury (Ciocchi *et al.*, 2010; Yu *et al.*, 2016; Wilson *et al.*, 2019), demonstrating that plasticity in the firing responses of these cells underlies changes in behavioral output. Whether the relative excitability of PKCδ$^+$ and Som$^+$ neurons is different at baseline conditions, however, has not been determined. To do this, we crossed *Prkcd*-Cre or *Sst*-Cre mice with an Ai9 reporter strain to obtain offspring that expressed the fluorescent protein tdTomato in cells expressing PKCδ or Somatostatin, respectively (**Figure 1A**). Using an acute brain slice preparation, we performed whole-cell patch-clamp recordings from a total of 124 visually identified fluorescent neurons in the right CeLC, corresponding to PKCδ$^+$ and Som$^+$ cells and distributed across the rostro-caudal extension of the CeLC (**Figure 1B and Figure 1-1**). Consistent with previous studies (Martina *et al.*, 1999; Schiess *et al.*, 1999; Lopez de Armentia & Sah, 2004; Chieng *et al.*, 2006), our experiments revealed that CeLC neurons display heterogeneous firing responses (**Figure 1C**). Thus, three discrete firing phenotypes are observed: spontaneously active (S), late-firing (LF), and regular-spiking (RS) neurons. Late-firing neurons are silent at rest, fire repetitively in response to a prolonged (500 ms) depolarizing current injection and have a substantial delay to firing action potentials, while regular-spiking cells are also silent at rest and fire repetitively in response to depolarizing current injections but have a much shorter onset to action potentials firing.

As illustrated in the representative traces in **Figure 1C**, all three firing types are readily observed in both PKCδ$^+$ and Som$^+$ CeLC neurons. Quantification of the proportion of cells with different firing types revealed, however, that the distribution of firing phenotypes is significantly different between PKCδ$^+$ and Som$^+$ cells (**Figure 1D**). Of the 75 PKCδ$^+$ cells recorded, for example, the majority (36/75; 48%) are regular-spiking neurons, whereas only 13 of the 49 (27%) Som$^+$ neurons

eNeuro Accepted Manuscript

recorded are regular-spiking. In marked contrast, most (27/49; 55%) of the Som$^+$ neurons recorded are spontaneously active at rest and only 20 of the 75 (27%) PKCδ$^+$ neurons recorded are spontaneously active. The remaining PKCδ$^+$ and Som$^+$ cells were late-firing and the proportion of this firing type, relative to the total cells, is similar between PKCδ$^+$ (19/75; 25%) and Som$^+$ (9/49; 18%) neurons. Together, these results demonstrate that while firing phenotypes are heterogeneous in PKCδ$^+$ and Som$^+$ CeLC cells, the proportion of cells with different firing types is cell-type-specific. The greater proportion of spontaneously active Som$^+$ cells suggests that these cells have a larger overall output compared to PKCδ$^+$ cells in the CeLC.

In the next set of experiments, we generated input-output curves to determine if the relative excitability of PKCδ$^+$ and Som$^+$ neurons is also different in late-firing and regular-spiking cells. Output in these experiments is defined as action potential firing rates in response to depolarizing current injections of increasing amplitudes. As illustrated in **Figure 2A**, prolonged (500 ms) depolarizing current injections elicited repetitive firing in both late-firing and regular-spiking PKCδ$^+$ and Som$^+$ neurons, with firing responses increasing as a function of the current injection amplitude in all four cell types. Evoked repetitive firing responses in late-firing and regular-spiking Som$^+$ neurons are significantly higher than in late-firing and regular-spiking PKCδ$^+$ cells, respectively, underscoring the notion that Som$^+$ cell output far outpaces that of PKCδ$^+$ neurons in the CeLC.

Consistent with the relative hyperexcitable phenotype of Som$^+$ late-firing neurons, compared to PKCδ$^+$ late-firing cells, the latency to first spike is significantly shorter in these cells (79.54 ± 7.32 ms), compared to PKCδ$^+$ late-firing cells (111.5 ± 6.23 ms) (**Figure 2B**). The minimal current amplitude that elicits an action potential (rheobase) as well as the voltage sag in response to a hyperpolarizing current injection, however, were indistinguishable between PKCδ$^+$ and Som$^+$ late-firing neurons (**Figure 2C and Figure 2-1**).

eNeuro Accepted Manuscript

Subthreshold membrane properties, like input resistance and resting membrane potential, can strongly influence the firing responses of a neuron in response to stimulation. To determine if subthreshold membrane properties contribute to the relative hyperexcitable phenotype of Som^+ CeLC neurons, we measured and compared these two parameters in $PKC\delta^+$ and Som^+ late-firing and regular-spiking neurons. Our analyses showed that input resistance is significantly higher in Som^+ (160.5 ± 10.23 MΩ) compared to $PKC\delta^+$ late-firing cells (131.4 ± 12.51 MΩ) (**Figure 2D**), suggesting that differences in subthreshold conductances might contribute to the differences in excitability observed in $PKC\delta^+$ and Som^+ neurons. Notably, the membrane potentials of late-firing Som^+ neurons (-84.44 ± 0.96 mV) are significantly hyperpolarized relative to the resting membrane potentials in $PKC\delta^+$ late-firing cells (-78.14 ± 1.37 mV) (**Figure 2E**), demonstrating that the greater excitability of late-firing Som^+ cells is independent of the resting membrane potential. In contrast, despite the pronounced differences in evoked firing responses of Som^+ and $PKC\delta^+$ regular-spiking neurons, all other passive and active membrane properties measured are indistinguishable between these two genetically distinct cell types (**Figure 2F-I and Figure 2-1**). Of note, however, in spite of the indistinguishable properties in regular-spiking neurons, the values for rheobase to fire action potentials in individual $PKC\delta^+$ neurons were non-normally distributed (**Figure 2G**), suggesting heterogeneity within this neuronal population.

Together, these results demonstrate that the output of Som^+ cells outpaces that of $PKC\delta^+$ cells in the CeLC but that the cellular mechanisms underlying the differences in excitability in Som^+ and $PKC\delta^+$ neurons are distinct for late-firing and regular-spiking cells.

$PKC\delta^+$, but not Som^+, CeLC neurons display accommodation of repetitive firing

Inter-spike interval (ISI) accommodation reflects the ability of neurons to sustain the frequency of firing in response to prolonged depolarizing input. The presence of ISI accommodation has been previously reported in CeLC neurons and has been

eNeuro Accepted Manuscript

497 widely used as a parameter to classify neurons in this brain region (Schiess *et al.*,
498 1999; Zhu & Pan, 2004; Hunt *et al.*, 2017).

499 To further determine if firing properties in the CeLC are cell-type-specific
500 and to gain additional insight into the mechanisms driving the differences in
501 excitability of these cells, we measured and compared ISI accommodation
502 between Som^+ and $PKC\delta^+$ CeLC neurons. Prolonged (500 ms) current injections
503 elicited repetitive firing in late-firing and regular-spiking Som^+ and $PKC\delta^+$ CeLC
504 neurons (**Figure 3A**). Quantification of the number of cells that display ISI
505 accommodation further revealed that approximately half of the late-firing and half of
506 the regular-spiking $PKC\delta^+$ neurons undergo ISI accommodation (**Figure 3B**). In
507 marked contrast, however, only one of the 21 Som^+ neurons analyzed exhibited ISI
508 accommodation in response to depolarizing current injection. The almost complete
509 lack of ISI accommodation in Som^+ neurons is consistent with the overall higher
510 output of these CeLC cells, compared to the $PKC\delta^+$ neurons. Further analyses of
511 firing responses, as well as passive and active membrane properties, in
512 accommodating and non-accommodating $PKC\delta^+$ neurons with either late-firing or
513 regular-spiking phenotypes revealed that some of these properties were different in
514 regular-spiking accommodating and non-accommodating neurons (**Table 1**). The
515 amplitude accommodation ratio between first and last spikes, for example, was
516 significantly smaller in accommodating $PKC\delta^+$ cells (0.7 ± 0.03) than in non-
517 accommodating $PKC\delta^+$ cells (0.8 ± 0.01). In addition, resting membrane potential
518 is significantly hyperpolarized in non-accommodating $PKC\delta^+$ cells (-77.4 ± 0.8 mV),
519 compared to accommodating $PKC\delta^+$ cells (-70.6 ± 1.8 mV). The differences in
520 resting potentials between accommodating and non-accommodating regular-
521 spiking neurons might contribute to the non-normal distribution of the resting
522 potential values that we measured in the pooled data from regular-spiking PKCδ+
523 neurons presented in **Figure 2I**.

524 All other properties measured in regular-spiking neurons and all properties
525 measured in late-firing neurons, however, were indistinguishable in $PKC\delta^+$ and
526 Som^+ neurons. Given the few differences in passive and active membrane within

eNeuro Accepted Manuscript

firing types, for the remainder of this study, accommodating and non-accommodating PKCδ$^+$ neurons were pooled and compared to non-accommodating Som$^+$ cells.

Frequency-dependent changes in spike amplitude, width and afterhyperpolarization (AHP) are three additional parameters used to measure the ability of neurons to sustain repetitive firing in response to prolonged depolarizing input. The presence of spike amplitude accommodation, spike broadening and AHP amplitude accommodation within an evoked train of action potentials are commonly used to classify and electrophysiologically characterize neurons in other brain regions, reflecting the repertoire of ion channels and ionic conductance of a cell (Bean, 2007). It is unknown, however, whether CeLC neurons display frequency-dependent changes in spike amplitude, width or AHP and, if they do, whether these changes are also cell-type-specific.

Measurements and comparisons of the amplitudes, widths and AHPs of the first and last spike within an evoked train of action potentials in late-firing and regular-spiking Som$^+$ and PKCδ$^+$ CeLC neurons demonstrated that all CeLC neurons display robust and significant frequency-dependent changes in spike amplitude, width and AHP amplitude in response to depolarizing current injections (**Figure 3C-H**). In all cells analyzed, for example, the amplitude of the last spike in an evoked train of action potentials is significantly shorter than the amplitude of the first spike within the same train (**Figure 3C-D**). Notably, while frequency-dependent shortening of the action potential is indistinguishable in PKCδ$^+$ and Som$^+$ regular-spiking neurons (**Figure 3D**), it is significantly larger in PKCδ$^+$ (0.58 ± 0.05) than in Som$^+$ late-firing cells (0.80 ± 0.04) (**Figure 3C**).

Quantification of action potential duration (APD) in the first and last spike further demonstrated that all four different cell types also exhibit robust APD accommodation, but that frequency-dependent APD broadening is indistinguishable between the different cell types (**Figure 3E-F**).

Finally, analysis of frequency-dependent AHP amplitude accommodation further revealed that all CeLC cell types exhibit significant AHP amplitude

eNeuro Accepted Manuscript

accommodation within an evoked train of action potentials and that AHP amplitude accommodation is significantly larger in Som^+ regular-spiking (0.83 ± 0.03) than in $PKC\delta^+$ regular-spiking neurons (0.91 ± 0.01) (**Figure 3G-H**).

Our combined results, showing that ISI accommodation in response to depolarizing current injections is selective to $PKC\delta^+$ neurons and that frequency-dependent spike amplitude accommodation is more robust in $PKC\delta^+$ than in Som^+, neurons demonstrates that the ability of $PKC\delta^+$ neurons to sustain firing in response to input is lower than that of Som^+ cells and that differences in intrinsic membrane properties at the suprathreshold level contribute to these differences. These results are consistent with the findings discussed in the previous sections of this study and suggest that firing phenotypes in the CeLC are cell-type-specific, with Som^+ cells displaying a larger overall output than $PKC\delta^+$ cells in the CeLC.

Action potential repolarization is slower in Som^+ than in $PKC\delta^+$ CeLC neurons

Suprathreshold membrane properties, including the membrane potential at which an action potential is initiated (voltage threshold) and the rates of depolarization and repolarization of individual action potentials can also strongly influence neuronal excitability (Bean, 2007). To gain additional insight into the mechanisms underlying the differences in the excitability of $PKC\delta^+$ and Som^+ cells, we examined the properties of single action potential waveforms elicited by a short (5 ms) depolarizing current injection in these cells (**Figure 4A**).

Consistent with the hyperexcitable phenotype of Som^+ late-firing neurons, the current amplitude required to induce an action potential (current threshold) is significantly smaller in Som^+ (1111 ± 56.31 pA) than $PKC\delta^+$ late-firing neurons (1758 ± 107.8 pA) (**Figure 4B**). Analyses of the depolarizing phase of the action potentials further demonstrated that voltage thresholds and rise times are indistinguishable between $PKC\delta^+$ and Som^+ late-firing cells (**Figure 4C-D**). In contrast, decay times are significantly longer, action potentials significantly prolonged and afterhyperpolarizations significantly depolarized in Som^+ (decay time, 0.74 ± 0.04 ms; action potential duration, 1.45 ± 0.03 ms; and

eNeuro Accepted Manuscript

afterhyperpolarization, -57.26 ± 1.46 mV) compared to PKCδ$^+$ neurons (decay time, 0.58 ± 0.01 ms; action potential duration, 1.25 ± 0.02 ms; and afterhyperpolarization, -60.25 ± 0.72 mV) (**Figure 4E-G**). These combined results demonstrate that while the depolarizing phase of action potentials is indistinguishable in PKCδ$^+$ and Som$^+$ late-firing CeLC neurons, the repolarizing phase is slower in Som$^+$ than in PKCδ$^+$ late-firing CeLC cells, likely contributing to the hyperexcitable phenotype observed in these cells.

Consistent with the indistinguishable subthreshold membrane properties and accommodation observed in PKCδ$^+$ and Som$^+$ regular-spiking CeLC neurons (**Figures 2 and 3**), most of the suprathreshold membrane properties measured are also indistinguishable in these cells (**Figure 4H-L**). An exception to this was the afterhyperpolarization in regular spiking neurons, which was significantly depolarized (-51.65 ± 0.76 mV) in Som$^+$ neurons compared with PKCδ$^+$ neurons (-56.37 ± 0.69 mV) (**Figure 4M**).

Together, these results suggest that differences in the intrinsic membrane properties of PKCδ$^+$ and Som$^+$ late-firing neurons contribute to the greater output of Som$^+$ late-firing cells. The differences in excitability in Som$^+$ and PKCδ$^+$ regular-spiking neurons, however, seems to be independent of the intrinsic membrane properties of the cells, further supporting that the cellular mechanisms underlying the greater output of Som$^+$ neurons are distinct for late-firing and regular-spiking CeLC cells.

Som$^+$ neurons display greater spontaneous firing rates and prolonged action potential durations compared to PKCδ$^+$ neurons

A substantial population of PKCδ$^+$ and Som$^+$ neurons are spontaneously active (Figure 1C-D). The next set of experiments aimed to further characterize the firing and intrinsic membrane properties of spontaneously active PKCδ$^+$ and Som$^+$ cells. As illustrated in Figure 5, both subtypes of neurons display low frequency spontaneous firing. Quantification of spontaneous firing rates revealed, however, that Som$^+$ spontaneously firing cells display higher firing frequencies (4.89 ± 0.60

eNeuro Accepted Manuscript

Hz) than PKCδ$^+$ cells (2.83 ± 0.39 Hz) (**Figure 5C**). Interspike potential, capacitance, and input resistance were indistinguishable between cells (**Figure 5D-F**). Analysis of single action potentials showed that while peak voltage and voltage threshold to fire an action potential are indistinguishable between Som$^+$ and PKCδ$^+$ neurons (**Figure 5G-H**), action potential durations are significantly prolonged in Som$^+$ neurons (1.27 ± 0.08 ms) compared to PKCδ$^+$ cells (0.92 ± 0.06 ms) (Figure 5K). Consistently, both rise and decay times are prolonged in Som$^+$ neurons compared to PKCδ$^+$ cells. Thus, the mean +/- SEM rise time was 0.51 ± 0.03 ms in Som$^+$ neurons, compared to only 0.40 ± 0.03 ms in PKCδ$^+$ cells (Figure 5I). Similarly, the mean +/- SEM decay time was 1.84 ± 0.19 ms in Som+ cells but only 1.0 ± 0.07 ms in PKCδ$^+$ neurons (**Figure 5J**). Afterhyperpolarization (AHP) amplitude of Som$^+$ neurons (-48.75 ± 0.89 mV) was also depolarized compared to AHP amplitude in PKCδ$^+$ neurons (-51.56 ± 1.25 mV) (**Figure 5L**).

Our combined results, demonstrating that Som$^+$ spontaneous neurons have greater firing frequencies than PKCδ$^+$ neurons, underscore the finding that Som$^+$ cells display greater excitability than PKCδ$^+$ neurons in the CeA, regardless of firing phenotype. The wider action potentials and depolarized afterhyperpolarizations observed in Som$^+$ neurons relative to PKCδ$^+$ cells suggest that the mechanisms underlying greater excitability in spontaneously active Som$^+$ neurons are different from those in late-firing and regular-spiking Som$^+$ cells.

Regular-spiking PKCδ$^+$ neurons excitability is dependent on the rostro-caudal anatomical localization within the CeC

Previous studies have shown that genetically distinct cells are differentially distributed throughout the CeLC (Han *et al.*, 2015; Kim *et al.*, 2017; McCullough *et al.*, 2018; Wilson *et al.*, 2019). As illustrated in **Figure 6**, and consistent with previous reports, for example, PKCδ$^+$ cells are localized mostly to the lateral (CeL) and capsular (CeC) subdivisions of the CeLC, while Som$^+$ cells are predominantly located in the CeL and medial subdivision (CeM) of the CeA (**Figure 6B**). Previous work has also demonstrated that although both cell types are found throughout the

eNeuro Accepted Manuscript

rostro-caudal axis, Som^+ expression is greater in the anterior amygdala and decreases posteriorly, while $PKC\delta^+$ cells are expressed more abundantly in the middle of the CeLC (**Figure 6B**) (Han *et al.*, 2015; Wilson *et al.*, 2019).

At the anatomical and electrophysiological levels, projection-specific neurons have been shown to be topographically organized within the CeLC and to exhibit distinct firing responses (Li & Sheets, 2018). It is unknown, however, whether the firing phenotypes of genetically distinct cells are dependent on their anatomical localization within the CeLC. We began to evaluate this by comparing the proportions of the three observed firing types (spontaneous, late-firing and regular-spiking; see **Figure 1**) in $PKC\delta^+$ and Som^+ cells localized to different subnuclei or rostro-caudal levels within the CeLC.

Our analyses revealed that firing types of all $PKC\delta^+$ and Som^+ cells are independent of their anatomical localization within the CeLC (**Table 2**). Further correlational analyses revealed, however, that the excitability of $PKC\delta^+$ regular-spiking neurons in the CeC correlates with the rostro-caudal localization of these cells (**Figure 7**). Thus, a significant positive correlation is seen for the number of spikes elicited in response to prolonged (500 ms) depolarizing current injection, with higher responses in neurons located in the posterior than in the anterior CeC (**Figure 7C**). Consistently, a significant negative correlation is observed for rheobase and latency to first spike, with lower values in neurons located in the posterior CeC, compared to neurons in the anterior CeC (**Figure 7D-E**). These rostro-caudal and subdivision-dependent differences in rheobase could contribute to the non-normal distribution of the values for rheobase that we measured in the pooled data from regular-spiking $PKC\delta^+$ neurons presented in **Figure 2G**. Firing responses to depolarizing current injections are indistinguishable in $PKC\delta^+$ regular-spiking neurons in the CeL as well as in all $PKC\delta^+$ late-firing neurons independently of their location within the rostro-caudal axis (**Figure 7C-E**).

eNeuro Accepted Manuscript

Together, these findings demonstrate that anatomical localization within the CeC is yet another source of heterogeneity that influences neuronal excitability in a cell-type specific manner in the CeA.

PKCδ$^+$ and Som$^+$ neurons are morphologically distinct

It is widely known that neuronal morphology and dendritic spines impact the electrophysiological properties, and therefore cellular output, of neurons (Connors & Regehr, 1996; Mainen & Sejnowski, 1996; Stiefel & Sejnowski, 2007). While previous studies have demonstrated that neurons in the CeLC are both morphologically and electrophysiologically heterogeneous (Martina *et al.*, 1999; Schiess *et al.*, 1999; Chieng *et al.*, 2006), a correlational link between the morphology and function of CeLC neurons is still missing.

Based on our electrophysiological findings demonstrating that excitability is markedly different in PKCδ$^+$ and Som$^+$ neurons in the right CeLC, we hypothesized that these two subpopulations of CeLC cells are also morphologically distinct. To test this hypothesis, we filled some of the neurons that were used for the electrophysiological studies by including biocytin in the recording pipette solution (**Figure 8A**). A total of 7 PKCδ$^+$ cells and 6 Som$^+$ biocytin-filled cells were successfully recovered and three-dimensionally reconstructed using this approach (**Figure 8B**).

Consistent with previous reports, the morphology of all CeLC neurons recovered resembled that of medium spiny neurons in the striatum. Notably, however, visual inspection of the reconstructed biocytin-filled neurons demonstrated that PKCδ$^+$ cells display more polarity (triangular or bipolar) than Som$^+$ cells, which have dendrites radiating in most directions outwards from the soma (**extended data files 1 and 2**). One PKCδ$^+$ cell (shown in grey in **Figure 8B**) was the only exception to this pattern. These qualitative observations suggested that the complexity of dendritic branching and dendritic length are different between PKCδ$^+$ and Som$^+$ CeLC neurons.

To quantify these qualitative differences in neuronal morphology, we performed Sholl analyses, which allows the quantification and comparison of the

eNeuro Accepted Manuscript

number of dendritic intersections as a function of distance from soma. The total number of primary, secondary and tertiary dendrites, as well as dendritic lengths and spine densities were also quantified in all cells. It is important to note, however, that given that these neurons were filled and reconstructed from coronal brain slices, the analyses presented here represent dendrites extending toward the dorsoventral and mediolateral direction and within the 250 µm thickness of the slice in the rostrocaudal direction.

As illustrated in **Figure 8C**, Sholl analyses revealed that the number of dendritic intersections is dependent on the distance from soma in both PKCδ$^+$ and Som$^+$ CeLC neurons, with maximal number of intersections observed at approximately 50 µm from the soma in both cell types. The number of dendritic intersections, however, was significantly higher in Som$^+$ than in PKCδ$^+$ neurons, demonstrating that dendritic arborizations are more complex in these cells compared to PKCδ$^+$ cells. Consistent with the observed polarity of PKCδ$^+$ cells, the total number of dendrites was significantly smaller in these neurons compared to the number of dendrites in Som$^+$ cells (**Figure 8D**). In addition, posthoc analysis revealed that both the number and length of dendrites increases as a function of branch order in Som$^+$ cells, but it is indistinguishable between primary, secondary, and tertiary dendrites of PKCδ$^+$ cells (**Figure 8D-E**). Lastly, while dendritic spine densities increased as a function of branching order in Som$^+$ neurons, it was indistinguishable between primary, secondary, and tertiary dendrites in PKCδ$^+$ cells (**Figure 8F**).

Together, these results demonstrate that neuronal morphology differs in genetically distinct subpopulations of cells in the CeLC, with more complex dendritic branching patterns observed in Som$^+$ neurons, than in PKCδ$^+$ cells.

The combined results from our electrophysiological and morphological reconstruction of PKCδ$^+$ and Som$^+$ CeLC neurons strongly suggest that the morphological properties of PKCδ$^+$ and Som$^+$ neurons contribute to the differences in excitability displayed by these two populations of CeLC cells, with more compact Som$^+$ neurons displaying higher excitability than the less compact PKCδ$^+$ cells. To

eNeuro Accepted Manuscript

test this hypothesis, we used patch-clamp electrophysiology to measure and compare whole-cell capacitance in PKCδ$^+$ and Som$^+$ CeLC neurons. Whole-cell capacitance is commonly used to measure the total surface area of a cell, and therefore, reflects the size or compactness of a neuron, with lower whole-cell capacitance seen in smaller, more compact neurons and vice versa.

Consistent with the results of our morphological reconstructions that show Som$^+$ neurons as more compact than PKCδ$^+$ CeLC neurons, our electrophysiological measurements revealed that whole-cell capacitance is significantly lower in Som$^+$ than in PKCδ$^+$ CeLC late-firing neurons (**Figure 8G**). Notably, the number of evoked spikes significantly correlated with whole-cell capacitance in both late-firing and regular-spiking cells, with greater number of spikes seen in neurons with lower whole-cell capacitance (**Figure 8H and J**). These results demonstrate that more compact CeLC neurons are more excitable than larger cells, establishing a direct link between the distinct morphological properties of PKCδ$^+$ and Som$^+$ CeLC neurons and their excitability output.

Nerve injury occludes differences in excitability between PKCδ$^+$ and Som$^+$ cells

The results of the experiments presented in **Figure 2**, performed in the absence of injury, show that Som$^+$ cells in the CeLC are hyperexcitable compared to PKCδ$^+$ neurons in this brain region. In a mouse model of neuropathic pain, however, previous studies have shown that nerve injury induces increases in the excitability of PKCδ$^+$ neurons but that, in complete contrast, it decreases the excitability of Som$^+$ CeLC cells (Wilson *et al.*, 2019). These results suggest that nerve injury affects the excitability differences normally seen in PKCδ$^+$ and Som$^+$ neurons, ultimately affecting the overall output gain in the CeA. Whether and how cell-type-specific changes in excitability following nerve injury affect the relative output of PKCδ$^+$ and Som$^+$ neurons in the CeLC remains unknown.

To investigate this, we used the mouse cuff model of neuropathic pain in combination with whole-cell patch-clamp in acute brain slices (**Figure 9A**). Consistent with previous reports using this neuropathic pain model (Benbouzid *et*

eNeuro Accepted Manuscript

762 *al.*, 2008; Wilson *et al.*, 2019), cuff implantation on the left sciatic nerve elicited
763 robust and significant hypersensitivity to cold, heat and tactile stimulation in the
764 hindpaw ipsilateral to treatment compared to the paw contralateral to cuff
765 placement (**Figure 9A**). Cold, heat and tactile hypersensitivity were assessed
766 using the acetone, Hargreaves and von-Frey tests, respectively.

767 As illustrated in **Figure 9B**, and similar to what is seen in uninjured
768 conditions (**Figure 2**), prolonged (500 ms) depolarizing current injections elicited
769 repetitive firing in all four CeLC cell types following injury, with the number of
770 evoked spikes increasing as a function of current injection amplitude. Notably,
771 however, the number of spikes in response to prolonged depolarizing current
772 injections is indistinguishable in PKCδ$^+$ and Som$^+$ neurons following injury, in both
773 late-firing and regular-spiking cells. This is in marked contrast to the pronounced
774 differences seen in uninjured animals (**Figure 2**) and demonstrates that nerve
775 injury occludes differences in excitability between PKCδ$^+$ and Som$^+$ cells in the
776 CeLC. Notably, the loss of difference in excitability is primarily due to an increase
777 in excitability of PKCδ$^+$ neurons following nerve injury, suggesting differential
778 engagement of CeLC neuronal populations in different conditions. Importantly, the
779 differences in evoked firing responses between PKCδ$^+$ and Som$^+$ late-firing
780 neurons is dependent on the amplitude of the depolarizing current injected (**Figure**
781 **9C**). Thus, while the number of spikes elicited by high amplitude (360 pA) current
782 injection is indistinguishable in PKCδ$^+$ and Som$^+$ late-firing neurons, firing
783 responses to low amplitude (180) current injections were significantly lower in
784 Som$^+$ than in PKCδ$^+$ neurons in the CeLC. Firing responses of regular-spiking
785 neurons, in contrast, were indistinguishable independently of the amplitude of
786 current injected, supporting further that the mechanisms driving excitability of late-
787 firing and regular-spiking neurons are distinct.

788 Consistent with the nerve injury-induced masking of neuronal excitability
789 differences in PKCδ$^+$ and Som$^+$ CeLC neurons, the differences in resting
790 membrane potential, input resistance, and latency to fire that we observed between

eNeuro Accepted Manuscript

PKCδ$^+$ and Som$^+$ CeLC late-firing neurons in uninjured conditions (**Figure 2B-E**) were also occluded in PKCδ$^+$ and Som$^+$ cells following nerve injury (**Figure 9-1**).

Together, these results demonstrate that following nerve injury, the relative excitability of PKCδ$^+$ and Som$^+$ cells is disrupted. These data suggest that within different contexts, CeLC neuronal populations are differentially engaged and thus affect the contribution of these cells to overall output in the CeLC.

DISCUSSION

The CeLC has been recently hailed as a critical hub for modulating an array of behaviors, ranging from food-seeking to pain responses (Neugebauer *et al.*, 2004; Janak & Tye, 2015; Kim *et al.*, 2017). The two predominantly expressed cell types in the CeLC, PKCδ$^+$ and Som$^+$ cells, have been shown to modulate many of these behaviors, often in opposing ways (Ciocchi *et al.*, 2010; Haubensak *et al.*, 2010; Li *et al.*, 2013; Wilson *et al.*, 2019). In the present study, we show that PKCδ$^+$ and Som$^+$ CeLC neurons have different electrophysiological and morphological properties, supporting their distinct and diverse range of function. The results from our experiments demonstrate that while the firing phenotypes of these two genetically distinct CeLC cell types are heterogeneous, there is a marked difference between the excitability of these cells, with Som$^+$ neurons displaying a much greater output than PKCδ$^+$ neurons.

In addition to the marked differences in excitability, our biocytin-based morphological reconstructions demonstrate that PKCδ$^+$ and Som$^+$ CeLC neurons are morphologically distinct, with more complex dendritic arborization patterns seen in Som$^+$ than in PKCδ$^+$ neurons. Importantly, our last set of experiments demonstrates that differences in the excitability of PKCδ$^+$ and Som$^+$ neurons are occluded in a mouse model of neuropathic pain, suggesting that maladaptive plastic changes that alter the relative output of CeLC cell types underlies the differential modulation of CeA-dependent behavior by these cells.

Together, the findings presented here identify fundamentally important differences in PKCδ$^+$ and Som$^+$ neurons that support the functional heterogeneity

eNeuro Accepted Manuscript

in the CeLC, shedding insight into how distinct subpopulations of neurons within this small brain structure can differentially contribute to the modulation of multiple behavioral outputs.

Greater output is a common feature of Som$^+$ CeLC neurons of all firing types

Previous studies have demonstrated that PKCδ$^+$ and Som$^+$ CeLC neurons have distinct, and often opposite, functions in the modulation of behaviors (Janak & Tye, 2015; Kim *et al.*, 2017; Wilson *et al.*, 2019). The cellular features that distinguish these two functionally distinct populations of CeLC neurons, however, are unknown. The results presented here demonstrate that PKCδ$^+$ and Som$^+$ neurons are electrophysiologically distinct. Despite the heterogeneity in firing responses in both cell types (**Figure 1**), a common and robust feature of all Som$^+$ CeLC neurons is that they exhibit greater firing responses than PKCδ$^+$ neurons within the same firing type (**Figure 2 and Figure 5**). This is important because it suggests that the firing responses to input, as well as the overall output of these cells are distinct, demonstrating that information processing is different in PKCδ$^+$ and Som$^+$ cells at baseline. Differences in how these cells respond to input might, therefore, contribute to their selective or differential influence on behavioral outputs.

Identifying the source of cell-type-specific differential excitability in the CeLC is a crucial step towards understanding their opposite function. The results from the experiments presented here suggest that there are multiple distinct sources for the cell-type-specific differential excitability of PKCδ$^+$ and Som$^+$ CeLC cells. Differences in both passive and active intrinsic membrane properties, for example, seem to drive the relative hyperexcitability in Som$^+$ late-firing neurons but do not contribute to the differences in excitability in regular-spiking cells (**Figures 2-4**). In contrast, changes in active, but not passive intrinsic membrane properties seem to underlie the relative hyperexcitability of Som+ spontaneously active cells (**Figure 5**). The greater input resistance, slower repolarization, shorter latencies and lower current thresholds for action potential generation, as well as the lack of ISI accommodation in late-firing Som+ neurons (compared to PKCδ$^+$) are consistent with differences in potassium conductances between these cells. Similarly, the

eNeuro Accepted Manuscript

hyperpolarized resting potential of late-firing Som+ neurons, relative to late-firing PKCδ$^+$ neurons suggest differences in the resting potassium conductance between these cells. On the other hand, the action potential broadening coupled with slower rise and decay durations and depolarized AHP amplitude in spontaneously active Som$^+$ cells (compared to PKCδ$^+$) suggests that differences in slowly inactivating sodium and fast-activating potassium currents underlie the relative hyperexcitability in these cells. Future investigation of the mechanism underlying the excitability differences between Som$^+$ and PKCδ$^+$ neurons is needed to further our understanding of functional heterogeneity within the CeA.

Our results demonstrate that regular-spiking Som$^+$ neurons are also much more excitable than PKCδ$^+$ regular-spiking CeLC cells but, unlike the late-firing neurons, most of the passive and active membrane properties are indistinguishable in these cells (**Figures 2-4**). Since synaptic blockers were not used in our experiments, these results suggest that the higher output in regular-spiking Som$^+$ neurons could be synaptically driven, which could result from higher excitatory inputs, lower inhibitory inputs, or a combination of both. The lateral and basolateral amygdala, as well as the lateral parabrachial nucleus are sources of excitatory inputs to the CeLC (Bernard & Besson, 1990; Lopez de Armentia & Sah, 2004). Previous work has demonstrated that both Som$^+$ and Som$^-$ CeLC cells receive monosynaptic excitatory inputs from these brain regions (Li *et al.*, 2013; Li & Sheets, 2019; Wilson *et al.*, 2019). In all these studies, however, glutamatergic inputs to Som$^-$ cells are stronger than those to Som$^+$ neurons in the CeC (Li *et al.*, 2013; Li & Sheets, 2019). Since PKCδ$^+$ and Som$^+$ neurons comprise most of the CeLC and are mutually exclusive (Li *et al.*, 2013; Kim *et al.*, 2017; Wilson *et al.*, 2019), it is likely that most of the Som$^-$ neurons that receive stronger monosynaptic excitatory inputs are PKCδ$^+$ cells. These results are somewhat counterintuitive because PKCδ$^+$ cells show lower excitability than Som$^+$ CeLC neurons, suggesting that differences in excitatory inputs do not contribute to higher excitability in Som$^+$ CeLC neurons. Previous reports show, however, that PKCδ$^+$ and Som$^+$ CeLC neurons are interconnected and inhibit each other (Haubensak *et al.*, 2010; Hunt *et*

eNeuro Accepted Manuscript

al., 2017), raising the possibility that differences in inhibitory inputs at the microcircuit level might contribute to the higher output of Som^+ CeLC neurons. An important variable to consider when trying to integrate the results of the present study with the results of the synaptic studies mentioned above is that the experiments described here were conducted in the dark phase of the cycle whereas the synaptic experiments referenced above were performed in the light phase of the cycle. This is particularly important given recent work demonstrating that the sleep-wake state of an animal influences the activity of CeLC neurons (Ma *et al.*, 2019). Defining the intrinsic and synaptic mechanisms underlying the differences in excitability between genetically distinct cells in the CeLC will be essential to fully understand their differential function in the modulation of behaviors.

Cell-type-specific morphology as a predictor of function

CeLC neurons have been morphologically defined as medium spiny neurons with heterogeneous dendritic branching complexities (Martina *et al.*, 1999; Schiess *et al.*, 1999; Chieng *et al.*, 2006). Our biocytin-based morphological reconstruction of $PKC\delta^+$ and Som^+ CeLC neurons revealed distinct morphological features in these cells (**Figure 8**). These results are surprising given the heterogeneous firing phenotypes of these genetically distinct populations of cells (**Figure 1**) but, at the same time, are consistent with previous studies that have failed to correlate morphological properties of CeLC neurons with firing phenotypes (Schiess *et al.*, 1999; Chieng *et al.*, 2006; Amano *et al.*, 2012).

The two common distinguishing features we found between Som^+ and $PKC\delta^+$ CeLC neurons are their morphology and relative excitability. Thus, Som^+ neurons are more compact, with lower whole-cell capacitance, a more complex dendritic branching pattern and a much greater overall firing output. $PKC\delta^+$ neurons, in contrast, have fewer (but longer) dendrites, higher whole-cell capacitance and a much lower overall firing output than Som^+ neurons (**Figures 2 and 8 and extended data files 1 and 2**).

eNeuro Accepted Manuscript

Previous studies have shown similar correlations between morphology and excitability in striatal medium spiny and cortical pyramidal neurons (Gertler *et al.*, 2008; van der Velden *et al.*, 2012). Thus, neurons expressing the D2 dopamine receptor are compact, have lower whole-cell capacitance and are more excitable, (similar to our Som^+ neurons) than those expressing the D1 receptor (Gertler *et al.*, 2008). Similar to our findings in Som^+ CeLC neurons, in the apical dendrite of layer 2/3 pyramidal neurons, higher dendritic branching complexities have been reported to correlate with greater excitability (van der Velden *et al.*, 2012). Moreover, in cortical pyramidal neurons, higher complexity of dendritic branching complexity was shown to increase excitability by reducing ISI accommodation, which is consistent with the lack of ISI accommodation we see in Som^+ neurons (**Figure 3**). Together, these results demonstrate that cell-type-specific morphology is an important determinant of neuronal excitability in $PKC\delta^+$ and Som^+ CeLC neurons and can be used as a predictor of function in the CeA.

Pain-related changes in excitability exemplify the ability of $PKC\delta^+$ and Som^+ CeLC to undergo robust plasticity

Our cell-type-specific characterization of $PKC\delta^+$ and Som^+ cells in the CeLC demonstrated that the overall output of these two genetically distinct populations is different at baseline (**Figure 2**). In the context of pain, however, we found that these differences were occluded (**Figure 9**), highlighting the power of these cells to undergo plasticity. Our findings suggest that a disruption in the excitability equilibrium of $PKC\delta^+$ and Som^+ neurons, driven by an increase in $PKC\delta^+$ neuronal excitability, can lead to CeLC-mediated pathological states. Similar to the properties at baseline, whether these cell-type-specific injury-induced changes are generalizable across species, development, sex or other types of pain (i.e. inflammatory, visceral, cancer) and time-points after injury remains unknown. Similarly, it will be important to determine whether the relative excitability of these cells is differently affected in other behavioral contexts (i.e. food seeking behaviors, fear, drug reward and relapse, etc.).

eNeuro Accepted Manuscript

Biological and methodological considerations

Multiple studies have previously described the intrinsic membrane and morphological properties of unidentified CeA neurons (Martina *et al.*, 1999; Schiess *et al.*, 1999; Dumont *et al.*, 2002; Lopez de Armentia & Sah, 2004; Chieng *et al.*, 2006; Amano *et al.*, 2012). While our results in genetically distinct CeA cells are mostly consistent with previous results in unidentified neurons, there are some notable differences. For example, while previous studies report low-threshold bursting neurons in the CeA (Dumont *et al.*, 2002; Haubensak *et al.*, 2010; Hunt *et al.*, 2017; Li & Sheets, 2018), we did not encounter any low-threshold bursting cell in our recordings. A second important difference between our study and previous reports is that PKCδ$^+$ neurons have been previously described as mostly late-firing neurons in mice (Haubensak *et al.*, 2010), whereas we see clear heterogeneity in the firing types of these cells (**Figure 1**), consistent with previous reports in rats (Amano *et al.*, 2012).

These apparent discrepancies might stem from differences in the light/dark cycle stage used, as discussed in detail above. Previous studies have shown that an additional important source of between-studies variability in slice physiology experiments is the specific experimental conditions used, such as composition of solutions used while prepping the slices and during recordings as well as the temperature of recordings (Avegno *et al.*, 2019). Biological variables, such as animal model species, sex and age have also been shown to strongly influence intrinsic membrane properties (Dumont *et al.*, 2002). Biological and methodological differences between studies may, therefore, account for the between-studies differences. Whether the differences in the properties of PKCδ$^+$ and Som$^+$ CeA cells that we report here are translatable to other animal species, females, different developmental stage and light phase of the light/dark cycle remains to be determined. An additional methodological consideration to keep in mind when interpreting the results presented here is that neuronal output was measured in response to depolarizing current injected directly into the cells. Future studies

eNeuro Accepted Manuscript

967 evaluating the output of PKCδ$^+$ and Som$^+$ CeA to synaptic stimulations will be
968 needed to get a full picture of the distinguishing biological features of these cells.

969 Lateralization of function in the CeA in the context of pain has been
970 previously described (Carrasquillo and Gereau, 2008; Ji and Neugebauer, 2009;
971 Allen *et al*., 2020). Most central amygdala studies either indiscriminately use either
972 side of the brain and pool the data or don't report the side of the brain used in the
973 experiments. For this reason, whether the electrophysiological and morphological
974 properties of CeA neurons, as well as the anatomical distribution of genetically
975 distinct cells within the CeA varies as a function of the side of the brain remains
976 unknown. The experiments described here were all performed in the right
977 amygdala and the nerve injuries in the contralateral (left) sciatic nerve.

978 A final important source of between-studies variability might be the
979 mathematical definition (or lack of reported definition) of the electrophysiological
980 parameters measured and the criteria used for firing type classification. One of the
981 strengths in the present study is the development, use and report of mathematical
982 definitions for all parameters measured and for the classification of firing types.
983 Use and report of mathematical definitions in future studies will facilitate
984 comparison of findings between reports and labs.

985 **Concluding Remarks**

986 Together, the findings described here demonstrate that genetically distinct
987 CeLC neurons display cell-type-specific differences in firing output and dendritic
988 morphology. These results support the distinct, and often opposite, contribution of
989 PKCδ$^+$ and Som$^+$ CeLC neurons in the modulation of specific behavioral outputs
990 and set the foundation for future studies aimed identifying the cellular mechanisms
991 driving heterogeneity of function in the CeA.

eNeuro Accepted Manuscript

992 **FIGURE LEGENDS:**

993 **Figure 1. Firing phenotypes are heterogenous in PKCδ+ and Som+ CeLC**
994 **neurons. (A)** Strategy for labeling genetically distinct subpopulations of neurons.
995 Prkcd-Cre or Sst-Cre mice were crossed with Ai9 reporter mice to produce
996 offspring that express tdTomato fluorescent protein in either PKCδ+ or Som+ cells.
997 **(B)** Acute amygdala slices for patch clamp electrophysiology. Whole brains were
998 extracted and coronally sectioned. Bottom panels are low (left and middle) and
999 high (right) magnification images of CeA slices. The CeA was visually identified by
1000 the distinct fiber bundles outlining the nuclei using differential interference contrast
1001 (left). PKCδ+ cells or Som+ cells expressing tdTomato (red) were readily seen
1002 under fluorescent microscopy (middle and right). Right panels show high
1003 magnification images of individual CeLC cells, with fluorescent images and
1004 differential interference contrast images overlaid. Black arrows denote fluorescently
1005 labeled cells, while white arrows denote unlabeled cells. Scale bars for left and
1006 center panel are 200 μm, right panel scale bar is 10 μm. **(C)** Representative
1007 voltage recordings of spontaneously active (S) cells, late-firing (LF) and regular-
1008 spiking (RS) PKCδ+ (left) or Som+ (right) neurons. **(D)** Proportions of each firing
1009 phenotype within recorded PKCδ+ and Som+ cell populations. The distribution of
1010 firing phenotypes is significantly ($p = 0.0055$, Chi-square test) different between
1011 PKCδ+ and Som+ cell populations.

1012 **Figure 2. Anatomical location of electrophysiology recordings.** Rostro-caudal
1013 anatomical locations of recorded $PKC\delta^+$ (**A**) and Som^+ (**B**) cells, represented as a
1014 schematic of the CeLC, created using Paxinos & Franklin, 2008. The capsular
1015 (CeC) and lateral (CeL) subdivisions of the central amygdala are shown in green
1016 and blue, respectively. LF = late-firing; RS = regular-spiking; S = spontaneous.

1017 **Figure 3. Som^+ CeLC neurons are more excitable than $PKC\delta^+$ cells**. (**A**)
1018 Representative voltage traces of late-firing (top left) or regular-spiking (bottom left)
1019 $PKC\delta^+$ cells (black) or Som^+ cells (blue) in response to depolarizing current

eNeuro Accepted Manuscript

injections. Right panel shows the number of spikes elicited as a function of the current injection amplitude. ****p < 0.0001, **p < 0.0036, two-way ANOVA. (**B-F**) Latency to first spike (**B** and **F**), rheobase (**C** and **G**), input resistance (R_{in}) (**D** and **H**), and resting membrane potential (V_{rest}) (**E** and **I**) for late-firing (**B-E**) and regular-spiking (**F-I**) neurons. **p = 0.0039, unpaired two-tailed t-test; *p = 0.0308, Mann-Whitney U test; ***p = 0.0002, unpaired two-tailed t-test with Welch's correction. For PKCδ$^+$ cells: n = 16-19 cells for late-firing and n = 35-36 regular-spiking. For Som$^+$ cells: n = 9 for late-firing and n = 12 for regular-spiking. All values are expressed as mean +/- S.E.M.

Figure 4. Voltage sag is indistinguishable in PKCδ$^+$ and Som$^+$ cells. Representative traces of late-firing (top) and regular-spiking (bottom) neurons in response to a 500 ms hyperpolarizing current injection, with PKCδ$^+$ cells shown in black and Som$^+$ cells in blue. Values are reported as mean ± S.E.M. For PKCδ$^+$ cells: n = 18 cells for late-firing and n = 33 regular-spiking. For Som$^+$ cells: n = 9 for late-firing and n = 13 for regular-spiking. Voltage sag = V_{sag}

Figure 5. Accommodation is selective to PKCδ$^+$, but not Som$^+$, neurons. (**A**) Representative voltage records of PKCδ$^+$ accommodating (Ac, left) and non-accommodating (Na, center) cells and Som$^+$ Na cells (right) for late firing (top) regular spiking (bottom) cells. Pink annotations depict interspike interval (ISI) accommodation, green denotes spike amplitude accommodation, and purple shows afterhyperpolarization (AHP) amplitude accommodation. (**B**) The proportions of Na and Ac late-firing and regular- spiking PKCδ$^+$ and Som$^+$ cells. (**C-H**) Spike amplitude accommodation (**C-D**), action potential duration (APD) accommodation (**E-F**), and AHP amplitude accommodation (**G-H**) for late-firing (left) and regular-spiking (right) PKCδ$^+$ and Som$^+$ cells. ****p < 0.0001, ***p < 0.005, paired two-tailed t-test; **p = 0.0034, unpaired two-tailed t-test; *p = 0.0142, unpaired two-tailed t-test with Welch's correction. For PKCδ$^+$ cells: n = 14-16 cells

eNeuro Accepted Manuscript

for late-firing and n = 33-36 regular-spiking. For Som+ cells: n = 9 for late-firing and n = 12-13 for regular-spiking. All values are expressed as mean ± S.E.M.

Figure 6. Slower repolarization in Som$^+$, than in PKCδ$^+$, neurons. (**A**) Representative single action potentials (left) elicited by 5 ms depolarizing current injections, phase plots (right) and plots of the first derivatives as a function of time (middle) of late-firing (top) and regular-spiking PKCδ$^+$ (black) and Som$^+$ (blue) neurons. Insets depict expanded timescales. Single action potential analyses for late-firing (**B-G**) and regular-spiking (**H-M**) PKCδ$^+$ and Som$^+$ neurons. Current (**B** and **H**) and voltage (**C** and **I**) thresholds to fire a single action potential. Action potential rise time (**D** and **J**), action potential decay time (**E** and **K**), action potential duration (APD) (**F** and **L**) and aferhyperpolarization (AHP) amplitudes (**G** and **M**). ****p < 0.0001, unpaired two-tailed t-test with Welch's correction; $^{\#\#\#\#}$p < 0.0001, Mann-Whitney U test; *p = 0.0498, ***p = 0.0008, unpaired two-tailed t-test. For PKCδ$^+$ cells: n = 16 cells for late-firing and n = 31 regular-spiking. For Som$^+$ cells: n = 9 for late firing and n = 10 for regular spiking. All values are expressed as mean ± S.E.M.

Figure 7. Spontaneous Som$^+$ CeLC neurons are more active and fire longer action potentials than PKCδ$^+$ cells. Representative spontaneous action potentials of PKCδ$^+$ (**A**) and Som$^+$ (**B**) neurons. Insets depict expanded timescales of single action potentials. (**B-G**) and regular-spiking (**H-M**) PKCδ$^+$ and Som$^+$ neurons. Frequency of action potential firing (**C**), interspike potential (**D**), capacitance (**E**), input resistance (**F**), peak voltage (**G**), voltage threshold (**H**), rise (**I**), decay (**J**), duration (**K**), and afterhyperpolarization amplitudes (**L**) for PKCδ$^+$ and Som$^+$ cells. **p < 0.01, unpaired two-tailed t-test with Welch's correction; ***p < 0.001, unpaired two-tailed t-test; $^{\#\#\#}$p < 0.0002, unpaired two-tailed t-test with Welch's correction; ***p < 0.0001, unpaired two-tailed t-test with Welch's

eNeuro Accepted Manuscript

correction; $^{\#\#}p < 0.005$, unpaired two-tailed t-test. For PKCδ$^+$ cells: n = 10-18 cells. For Som$^+$ cells: n = 17-23 cells. All values are expressed as mean ± S.E.M.

Figure 8. Rostro-caudal distribution of PKCδ$^+$ and Som$^+$ neurons in the CeA. (**A**) Representative low (left) and high (second to fifth panels) magnification images of coronal CeA slices immunostained for PKCδ (PKCδ-IF, cyan), with cells positive for Som-tdTomato shown in red. Merged signals between PKCδ-IF and Som-tdTomato are shown in the fourth panels. Rightmost panels depict high-magnification images of areas delineated by the white box. Scale bars are 1 mm for left panels, 100 μm for middle panels, and 20 μm for right panels. (**B**) Mean ± S.E.M. number of cells positive for PKCδ (cyan), Som (red) or colabeled with both (white circles) in the capsular (CeC), lateral (CeL) or medial (CeM) subdivisions of the CeA, as well as the total number of positive cells, are shown as a function of the rostro-caudal distribution relative to Bregma. n = 1-8 slices per rostro-caudal level from a total of 2-10 mice.

Figure 9. Firing responses in regular-spiking PKCδ$^+$ neurons correlate with rostro-caudal anatomical location within the CeC. (**A**) Schematics of rostral, middle, and caudal regions of the CeLC, with the CeL represented in green and purple and the CeC represented in blue and pink. (**B**) Representative voltage traces of evoked firing responses in regular-spiking PKCδ$^+$ neurons in the rostral, middle and caudal CeC (top panel, blue) and CeL (bottom panel, green). (**C-E**) Correlational plots between the number of evoked action potentials (**C**), rheobase (**D**), or latency to fire (**E**) and the rostro-caudal location of regular spiking (top) and late-firing (bottom) cells. Prolong (500 ms) depolarizing current injections of 140 pA and 240 pA were used to evoke repetitive firing in regular-spiking and late-firing cells, respectively. For regular-spiking neurons in the CeC, there was a positive correlation between the number of evoked action potentials and the rostro-caudal level ($p = 0.0045$, $r^2 = 0.5031$, linear regression analysis) and a negative correlation between rheobase ($p = 0.0036$, $r^2 = 0.5193$, linear regression analysis) and latency

eNeuro Accepted Manuscript

to first spike ($p = 0.0118$, $r^2 = 0.4858$, linear regression analysis) with the rostro-caudal level. None of the measured parameters in the CeL and in late-firing cells in the CeC correlated with the rostro-caudal level. For CeL: n = 7 cells for late-firing and n = 18 for regular-spiking. For CeC: n = 10 for late-firing and n = 14 for regular-spiking.

Figure 10. PKCδ$^+$ and Som$^+$ cells are morphologically distinct. (**A**) Morphological reconstruction of biocytin-filled cells in acute brain slices. CeLC cells were filled with biocytin during whole-cell patch-clamp recordings in acute amygdala slices. Representative images of biocytin-filled PKCδ$^+$ and Som$^+$ cells are shown in cyan in the right panel. Scale bars = 100 µm. (**B**) Morphological reconstruction of PKCδ$^+$ (top) and Som$^+$ biocytin-filled neurons. Scale bar = 100 µm. (**C**) Sholl analysis for number of dendritic intersections as a function of radial distance from soma. (**D-F**) Numbers (**D**), lengths (**E**), and spine densities (**F**) of primary (1º), secondary (2º), and tertiary (3º) dendrites for PKCδ$^+$ and Som$^+$ CeA cells. $^{**}p < 0.01$, two-way ANOVA. (**G** and **I**) Whole-cell membrane capacitance for late-firing (**G**) and regular-spiking (**I**) PKCδ$^+$ and Som$^+$ CeA cells. (**H** and **J**) Correlational plots between the number of action potentials evoked in response to prolonged (500 ms) depolarizing current injections of either 140 (regular-spiking) or 240 pA (late-firing) and whole-cell membrane capacitance in late-firing (**H**) and regular-spiking (**J**) PKCδ$^+$ (black) and Som$^+$ (blue) CeA cells. A negative correlation was found in both late-firing ($p = 0.0039$, $r^2 = 0.29$, linear regression analysis) and regular-spiking ($p < 0.0001$, $r^2 = 0.32$, linear regression analysis) neurons. For PKCδ$^+$ cells: n = 7 cells for morphology; n = 18-19 late-firing and n = 35-36 for regular-spiking. For Som$^+$ cells: n = 6 cells for morphology; n = 9 late-firing and n = 13 for regular-spiking. All values are expressed as mean ± S.E.M.

Figure 11. Excitability differences between PKCδ$^+$ and Som$^+$ cells are occluded in the context of persistent pathological pain. (**A**) Cuff model of neuropathic pain used in electrophysiological experiments. Following placement of the sciatic nerve cuff, mice developed hypersensitivity to cold (acetone test), heat

eNeuro Accepted Manuscript

(Hargreaves test), and tactile (von Frey test) stimulation on hindpaws contralateral to nerve injury, compared to the ipsilateral hindpaws. Acute brain slices for electrophysiological experiments were collected following cuff placement in the sciatic nerve of *Prkcd*-Cre::Ai9 or *Sst*-Cre::Ai9 mice. (**B**) Representative voltage recordings of late-firing (top) and regular-spiking (bottom) PKCδ$^+$ (black) and Som$^+$ (blue) cells in response to depolarizing current injections. Right panels show the number of spikes elicited as a function of the current injection amplitude. (**C**) The number of action potentials elicited in response to 180 pA and 360 pA depolarizing current injections in late-firing (top) and regular-spiking (bottom) PKCδ$^+$ (black) and Som$^+$ (blue) CeA cells. ****p < 0.0001, ***p < 0.0002, *p = 0.0314, Mann-Whitney U test. n = 8-21 mice for behavioral tests. For PKCδ$^+$ cells: n = 11-12 late-firing and n = 16-18 for regular-spiking. For Som$^+$ cells: n = 7 late-firing and n = 20-21 for regular-spiking. All values are expressed as mean ± S.E.M.

Figure 12. Passive membrane and repetitive firing properties of PKCδ$^+$ and Som$^+$ cells following nerve injury. All data are reported as mean ± S.E.M. For PKCδ$^+$ cells: n = 12 cells for late-firing and n = 18 regular-spiking. For Som$^+$ cells: n = 6-7 for late-firing and n = 21 for regular-spiking. V_{rest} = resting membrane potential; R_{in} = input resistance.

Table 1. Passive membrane, repetitive firing, and single action potential properties of PKCδ$^+$ non-accommodating and accommodating cells. All values are expressed as mean ± S.E.M. *p=0.0063, unpaired two-tailed t-test, comparing V_{rest} in regular-spiking accommodating and non-accommodating PKCδ$^+$ cells. **p=0.0003, Mann Whitney U test, comparing ISI accommodation in accommodating and non-accommodating late-firing PKCδ$^+$ cells; ***p<0.0001, unpaired two tailed t-test, comparing ISI accommodation in accommodating and non-accommodating regular-spiking PKCδ$^+$ cells; $^{\#}$p<0.0001, unpaired two-tailed t-test with Welch's correction, comparing amplitude accommodation in regular-spiking PKCδ$^+$ cells. V_{rest} = resting membrane potential; R_{in} = input resistance; ISI = inter-spike interval; AHP = afterhyperpolarization.

eNeuro Accepted Manuscript

Table 2. Firing phenotypes of PKCδ$^+$ and Som$^+$ CeLC cells by anatomical location. Proportions of cells with different firing phenotypes are shown for PKCδ$^+$ and Som$^+$ neurons in the capsular (CeC) and lateral (CeL) subdivisions of the central amygdala (CeA). Anterior is defined as the CeA between bregma -0.94 and bregma -1.34; middle as the CeA at bregma -1.46; and posterior as the CeA between bregma -1.58 and bregma -1.94. S = spontaneous; LF = late-firing; RS = regular-spiking; CeC = capsular subdivision of the central amygdala; CeL = lateral subdivision of the central amygdala.

Table 3. Statistical Analyses. Detailed information about data structure, statistical tests and results, and sample sizes. LF: late-firing; RS: regular spiking; IF: current-frequency plot; RM: repeated measures; F(DFn, DFd): degree of freedom for the numerator of the F ratio, for the denominator of the F ratio; df: degrees of freedom; Rin: input resistance; Vrest: resting membrane potential; AHP: afterhyperpolarization; Ithreshold: current threshold; Vthreshold: voltage threshold; IS: interspike; AP: action potential; Na: non-accommodating; Ac: accommodating; ISI: interspike interval; Vsag: voltage sag.

REFERENCES

Aggleton JP. (2000). *The amygdala : a functional analysis*. Oxford University Press, New York.

Amano T, Amir A, Goswami S & Pare D. (2012). Morphology, PKCdelta expression, and synaptic responsiveness of different types of rat central lateral amygdala neurons. *J Neurophysiol* **108,** 3196-3205.

Avegno EM, Middleton JW & Gilpin NW. (2019). Synaptic GABAergic transmission in the central amygdala (CeA) of rats depends on slice preparation and recording conditions. *Physiol Rep* **7,** e14245.

Bean BP. (2007). The action potential in mammalian central neurons. *Nat Rev Neurosci* **8,** 451-465.

eNeuro Accepted Manuscript

Benbouzid M, Pallage V, Rajalu M, Waltisperger E, Doridot S, Poisbeau P, Freund-Mercier MJ & Barrot M. (2008). Sciatic nerve cuffing in mice: a model of sustained neuropathic pain. *Eur J Pain* **12,** 591-599.

Bernard JF & Besson JM. (1990). The spino(trigemino)pontoamygdaloid pathway: electrophysiological evidence for an involvement in pain processes. *J Neurophysiol* **63,** 473-490.

Carrasquillo Y & Gereau IV RW. (2007). Activation of the extracellular signal-regulated kinase in the amygdala modulates pain perception. *J Neurosci* **27,** 1543-1551.

Chieng BC, Christie MJ & Osborne PB. (2006). Characterization of neurons in the rat central nucleus of the amygdala: cellular physiology, morphology, and opioid sensitivity. *J Comp Neurol* **497,** 910-927.

Choi Y, Yoon YW, Na HS, Kim SH & Chung JM. (1994). Behavioral signs of ongoing pain and cold allodynia in a rat model of neuropathic pain. *Pain* **59,** 369-376.

Ciocchi S, Herry C, Grenier F, Wolff SB, Letzkus JJ, Vlachos I, Ehrlich I, Sprengel R, Deisseroth K, Stadler MB, Muller C & Luthi A. (2010). Encoding of conditioned fear in central amygdala inhibitory circuits. *Nature* **468,** 277-282.

Colburn RW, Lubin ML, Stone DJ, Jr., Wang Y, Lawrence D, D'Andrea MR, Brandt MR, Liu Y, Flores CM & Qin N. (2007). Attenuated cold sensitivity in TRPM8 null mice. *Neuron* **54,** 379-386.

Connors BW & Regehr WG. (1996). Neuronal firing: does function follow form? *Curr Biol* **6,** 1560-1562.

Costantini I, Ghobril JP, Di Giovanna AP, Allegra Mascaro AL, Silvestri L, Mullenbroich MC, Onofri L, Conti V, Vanzi F, Sacconi L, Guerrini R, Markram H, Iannello G & Pavone FS. (2015). A versatile clearing agent for multi-modal brain imaging. *Sci Rep* **5,** 9808.

eNeuro Accepted Manuscript

1223 Davis M & Whalen PJ. (2001). The amygdala: vigilance and emotion. *Mol Psychiatry* **6,** 13-
1224 34.

1225

1226 Dumont EC, Martina M, Samson RD, Drolet G & Pare D. (2002). Physiological properties
1227 of central amygdala neurons: species differences. *Eur J Neurosci* **15,** 545-552.

1228

1229 Franklin KBJ & Paxinos G. (2008). *The mouse brain in stereotaxic coordinates*. Boston :
1230 Elsevier/Academic Press, Amsterdam ;.

1231

1232 Gertler TS, Chan CS & Surmeier DJ. (2008). Dichotomous anatomical properties of adult
1233 striatal medium spiny neurons. *J Neurosci* **28,** 10814-10824.

1234

1235 Gilpin NW, Herman MA & Roberto M. (2015). The central amygdala as an integrative hub
1236 for anxiety and alcohol use disorders. *Biol Psychiatry* **77,** 859-869.

1237

1238 Gong S, Doughty M, Harbaugh CR, Cummins A, Hatten ME, Heintz N & Gerfen CR.
1239 (2007). Targeting Cre recombinase to specific neuron populations with bacterial artificial
1240 chromosome constructs. *J Neurosci* **27,** 9817-9823.

1241

1242 Gong S, Zheng C, Doughty ML, Losos K, Didkovsky N, Schambra UB, Nowak NJ, Joyner
1243 A, Leblanc G, Hatten ME & Heintz N. (2003). A gene expression atlas of the central
1244 nervous system based on bacterial artificial chromosomes. *Nature* **425,** 917-925.

1245

1246 Han S, Soleiman MT, Soden ME, Zweifel LS & Palmiter RD. (2015). Elucidating an
1247 Affective Pain Circuit that Creates a Threat Memory. *Cell* **162,** 363-374.

1248

1249 Hargreaves K, Dubner R, Brown F, Flores C & Joris J. (1988). A new and sensitive method
1250 for measuring thermal nociception in cutaneous hyperalgesia. *Pain* **32,** 77-88.

1251

1252 Haubensak W, Kunwar PS, Cai H, Ciocchi S, Wall NR, Ponnusamy R, Biag J, Dong HW,
1253 Deisseroth K, Callaway EM, Fanselow MS, Luthi A & Anderson DJ. (2010). Genetic
1254 dissection of an amygdala microcircuit that gates conditioned fear. *Nature* **468,** 270-276.

1255

eNeuro Accepted Manuscript

1256 He M, Liu Y, Wang X, Zhang MQ, Hannon GJ & Huang ZJ. (2012). Cell-type-based
1257 analysis of microRNA profiles in the mouse brain. *Neuron* **73,** 35-48.

1258

1259 Hunt S, Sun Y, Kucukdereli H, Klein R & Sah P. (2017). Intrinsic Circuits in the Lateral
1260 Central Amygdala. *eNeuro* **4**.

1261

1262 Hurst JL & West RS. (2010). Taming anxiety in laboratory mice. *Nat Methods* **7,** 825-826.

1263

1264 Janak PH & Tye KM. (2015). From circuits to behaviour in the amygdala. *Nature* **517,** 284-
1265 292.

1266

1267 Kim J, Zhang X, Muralidhar S, LeBlanc SA & Tonegawa S. (2017). Basolateral to Central
1268 Amygdala Neural Circuits for Appetitive Behaviors. *Neuron* **93,** 1464-1479 e1465.

1269

1270 Li H, Penzo MA, Taniguchi H, Kopec CD, Huang ZJ & Li B. (2013). Experience-dependent
1271 modification of a central amygdala fear circuit. *Nat Neurosci* **16,** 332-339.

1272

1273 Li JN & Sheets PL. (2018). The central amygdala to periaqueductal gray pathway
1274 comprises intrinsically distinct neurons differentially affected in a model of inflammatory
1275 pain. *J Physiol* **596,** 6289-6305.

1276

1277 Li JN & Sheets PL. (2019). Spared nerve injury differentially alters parabrachial
1278 monosynaptic excitatory inputs to molecularly specific neurons in distinct subregions of the
1279 central amygdala. *Pain*.

1280

1281 Lopez de Armentia M & Sah P. (2004). Firing properties and connectivity of neurons in the
1282 rat lateral central nucleus of the amygdala. *J Neurophysiol* **92,** 1285-1294.

1283

1284 Ma C, Zhong P, Liu D, Barger ZK, Zhou L, Chang WC, Kim B & Dan Y. (2019). Sleep
1285 Regulation by Neurotensinergic Neurons in a Thalamo-Amygdala Circuit. *Neuron* **103,**
1286 323-334 e327.

1287

eNeuro Accepted Manuscript

1288 Mainen ZF & Sejnowski TJ. (1996). Influence of dendritic structure on firing pattern in
1289 model neocortical neurons. *Nature* **382,** 363-366.

1290

1291 Martina M, Royer S & Pare D. (1999). Physiological properties of central medial and
1292 central lateral amygdala neurons. *J Neurophysiol* **82,** 1843-1854.

1293

1294 McCullough KM, Morrison FG, Hartmann J, Carlezon WA, Jr. & Ressler KJ. (2018).
1295 Quantified Coexpression Analysis of Central Amygdala Subpopulations. *eNeuro* **5**.

1296

1297 Neugebauer V, Li W, Bird GC & Han JS. (2004). The amygdala and persistent pain.
1298 *Neuroscientist* **10,** 221-234.

1299

1300 Paxinos G, Franklin KBJ & Franklin KBJ. (2001). *The mouse brain in stereotaxic*
1301 *coordinates*. Academic Press, San Diego.

1302

1303 Schiess MC, Callahan PM & Zheng H. (1999). Characterization of the electrophysiological
1304 and morphological properties of rat central amygdala neurons in vitro. *J Neurosci Res* **58,**
1305 663-673.

1306

1307 Stiefel KM & Sejnowski TJ. (2007). Mapping function onto neuronal morphology. *J*
1308 *Neurophysiol* **98,** 513-526.

1309

1310 Swietek B, Gupta A, Proddutur A & Santhakumar V. (2016). Immunostaining of Biocytin-
1311 filled and Processed Sections for Neurochemical Markers. *J Vis Exp*.

1312

1313 Taniguchi H, He M, Wu P, Kim S, Paik R, Sugino K, Kvitsiani D, Fu Y, Lu J, Lin Y, Miyoshi
1314 G, Shima Y, Fishell G, Nelson SB & Huang ZJ. (2011). A resource of Cre driver lines for
1315 genetic targeting of GABAergic neurons in cerebral cortex. *Neuron* **71,** 995-1013.

1316

1317 van der Velden L, van Hooft JA & Chameau P. (2012). Altered dendritic complexity affects
1318 firing properties of cortical layer 2/3 pyramidal neurons in mice lacking the 5-HT3A
1319 receptor. *J Neurophysiol* **108,** 1521-1528.

1320

eNeuro Accepted Manuscript

1321 Veinante P, Yalcin I & Barrot M. (2013). The amygdala between sensation and affect: a
1322 role in pain. *J Mol Psychiatry* **1,** 9.

1323

1324 Venniro M, Caprioli D, Zhang M, Whitaker LR, Zhang S, Warren BL, Cifani C, Marchant
1325 NJ, Yizhar O, Bossert JM, Chiamulera C, Morales M & Shaham Y. (2017). The Anterior
1326 Insular Cortex-->Central Amygdala Glutamatergic Pathway Is Critical to Relapse after
1327 Contingency Management. *Neuron* **96,** 414-427 e418.

1328

1329 Venniro M, Zhang M, Caprioli D, Hoots JK, Golden SA, Heins C, Morales M, Epstein DH &
1330 Shaham Y. (2018). Volitional social interaction prevents drug addiction in rat models. *Nat*
1331 *Neurosci* **21,** 1520-1529.

1332

1333 Wilson TD, Valdivia S, Khan A, Ahn HS, Adke AP, Gonzalez SM, Sugimura YK &
1334 Carrasquillo Y. (2019). Dual and Opposing Functions of the Central Amygdala in the
1335 Modulation of Pain. *Cell Rep* **29,** 332-346 e335.

1336

1337 Yu K, Garcia da Silva P, Albeanu DF & Li B. (2016). Central Amygdala Somatostatin
1338 Neurons Gate Passive and Active Defensive Behaviors. *J Neurosci* **36,** 6488-6496.

1339

1340 Zald DH. (2003). The human amygdala and the emotional evaluation of sensory stimuli.
1341 *Brain Res Brain Res Rev* **41,** 88-123.

1342

1343 Zhu W & Pan ZZ. (2004). Synaptic properties and postsynaptic opioid effects in rat central
1344 amygdala neurons. *Neuroscience* **127,** 871-879.

1345

1346

eNeuro Accepted Manuscript

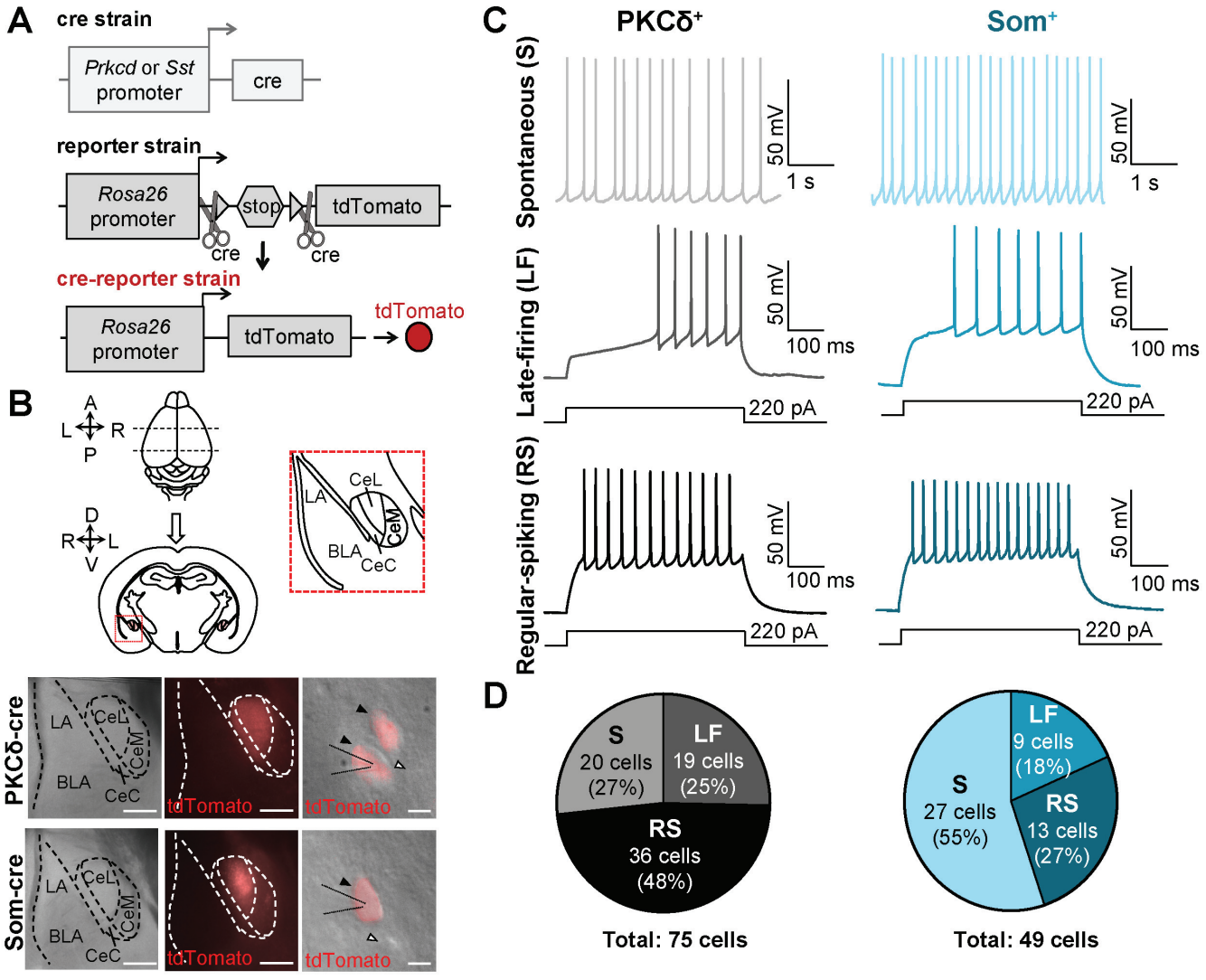

eNeuro Accepted Manuscript

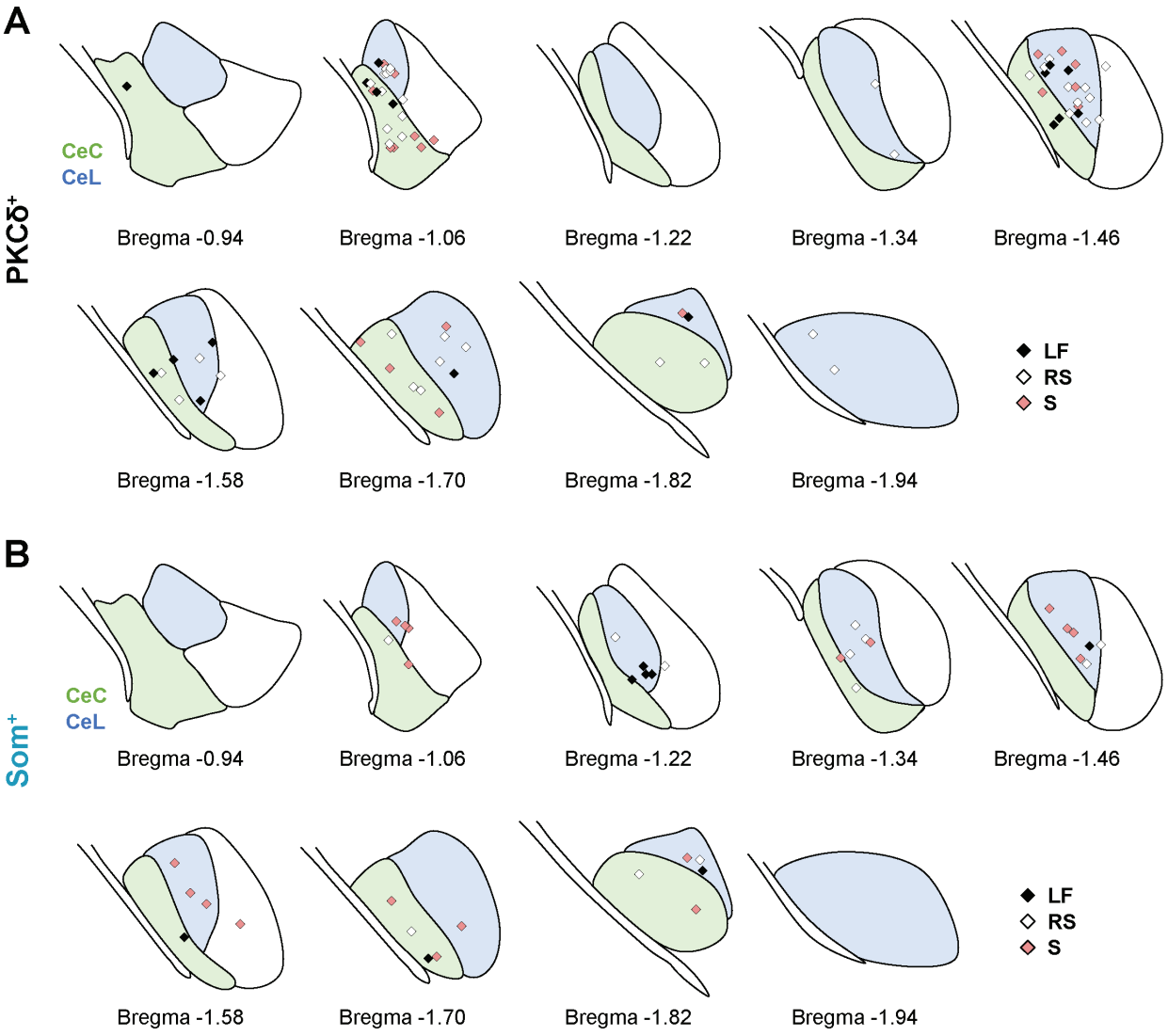

eNeuro Accepted Manuscript

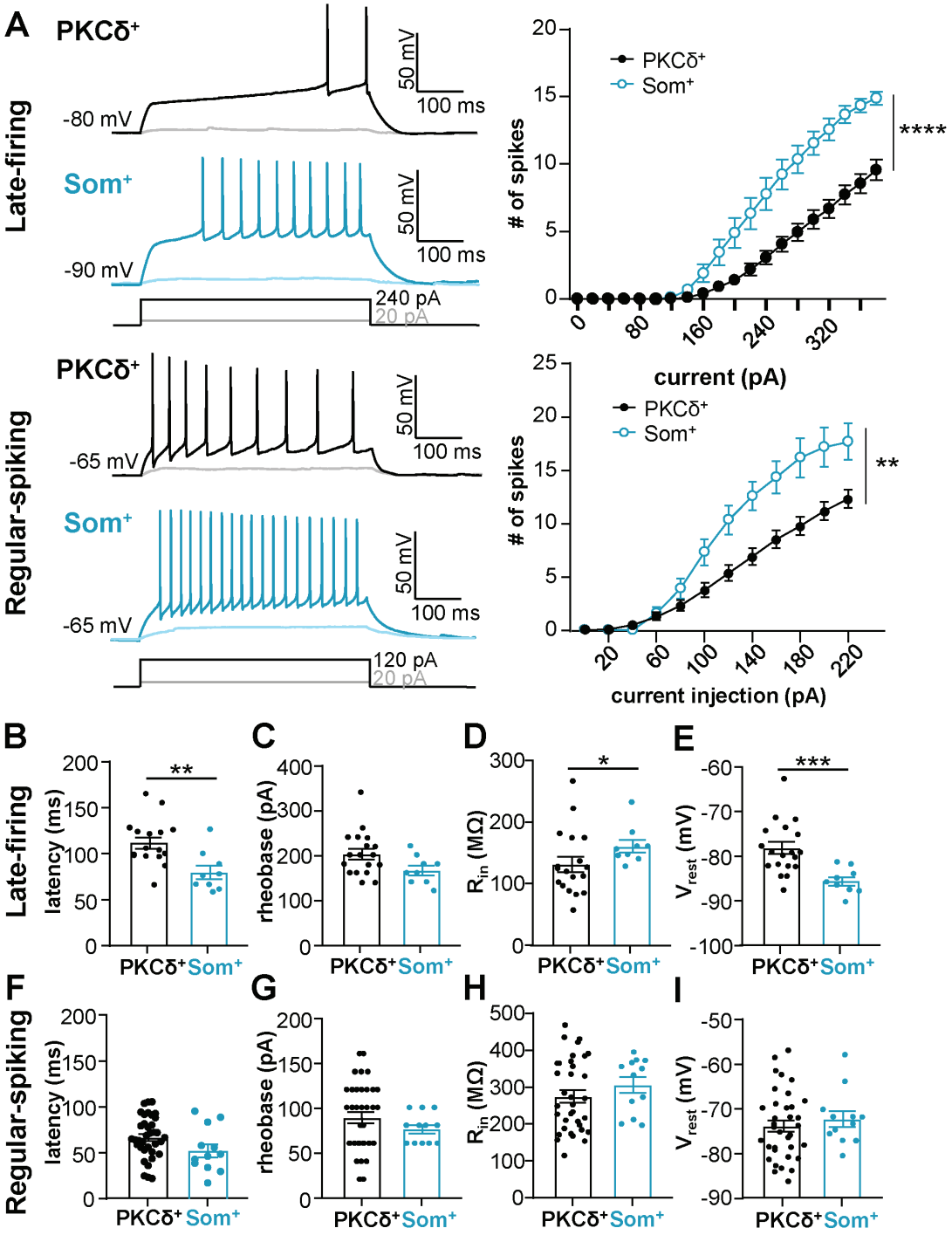

eNeuro Accepted Manuscript

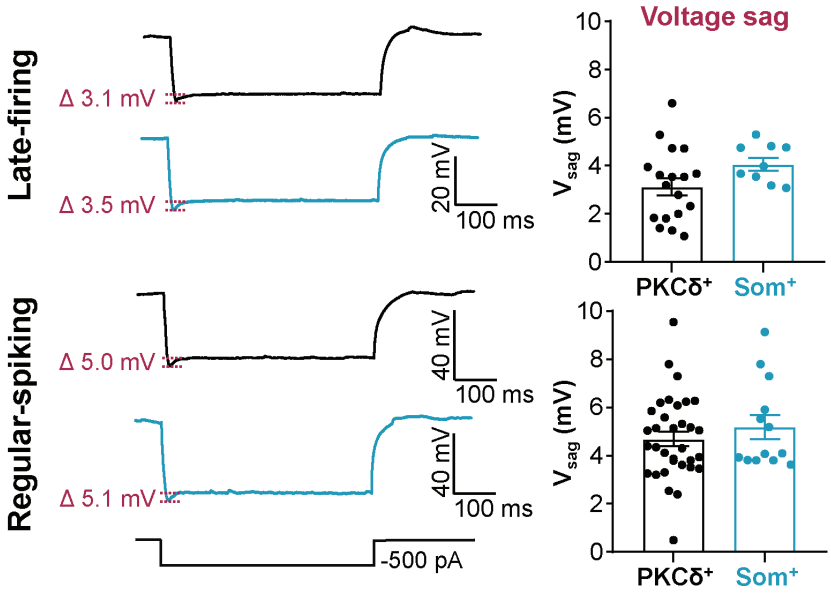

eNeuro Accepted Manuscript

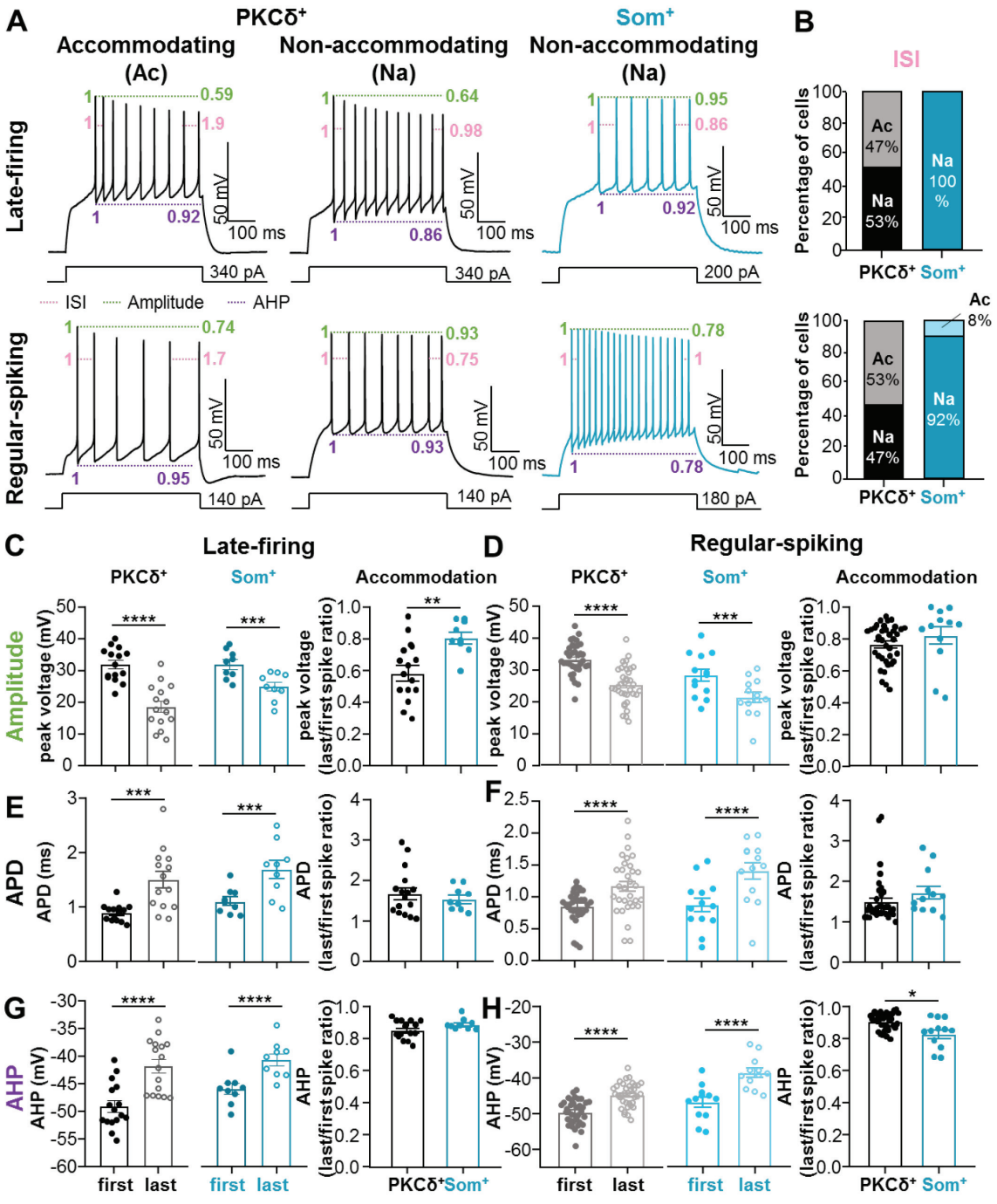

eNeuro Accepted Manuscript

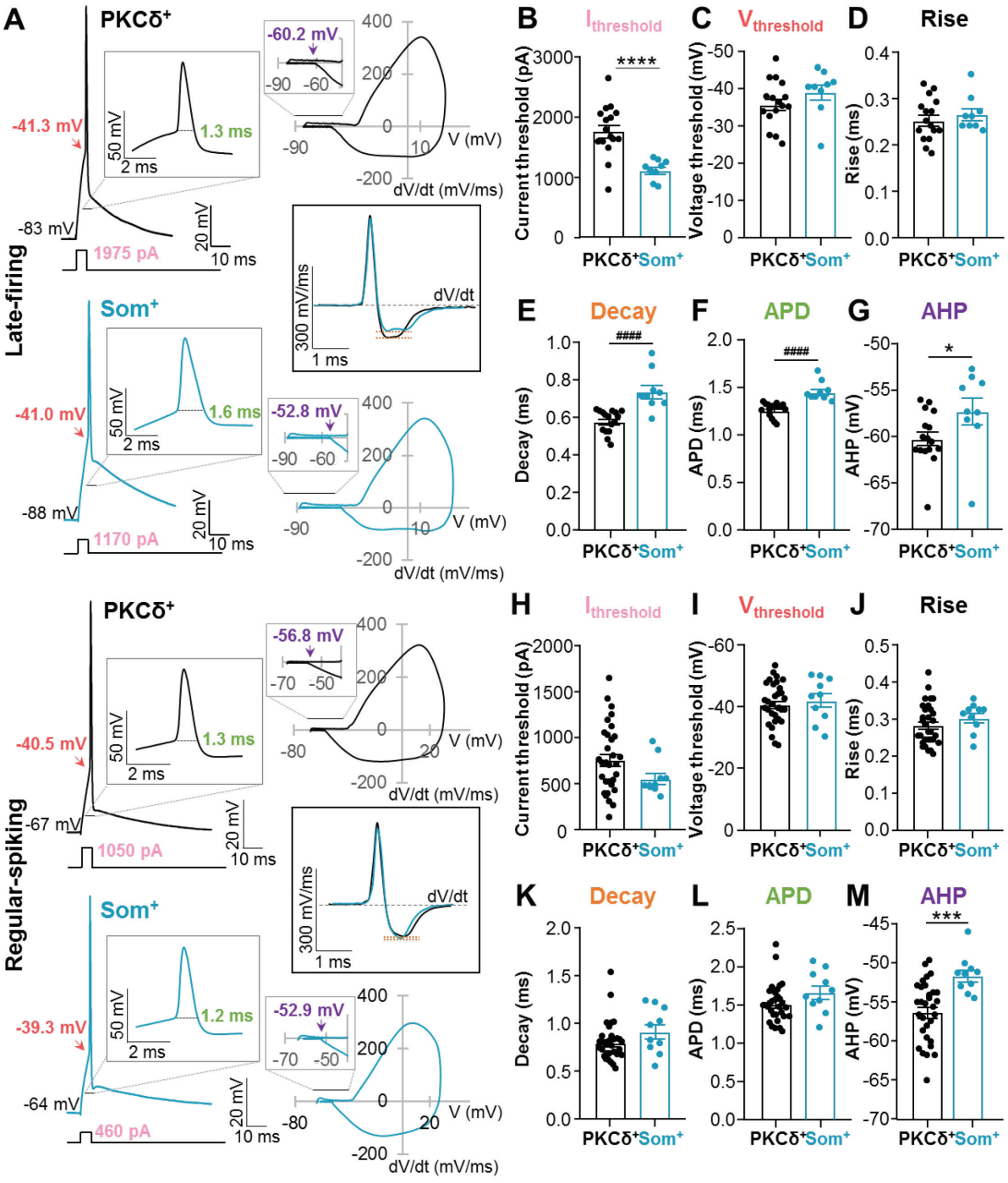

eNeuro Accepted Manuscript

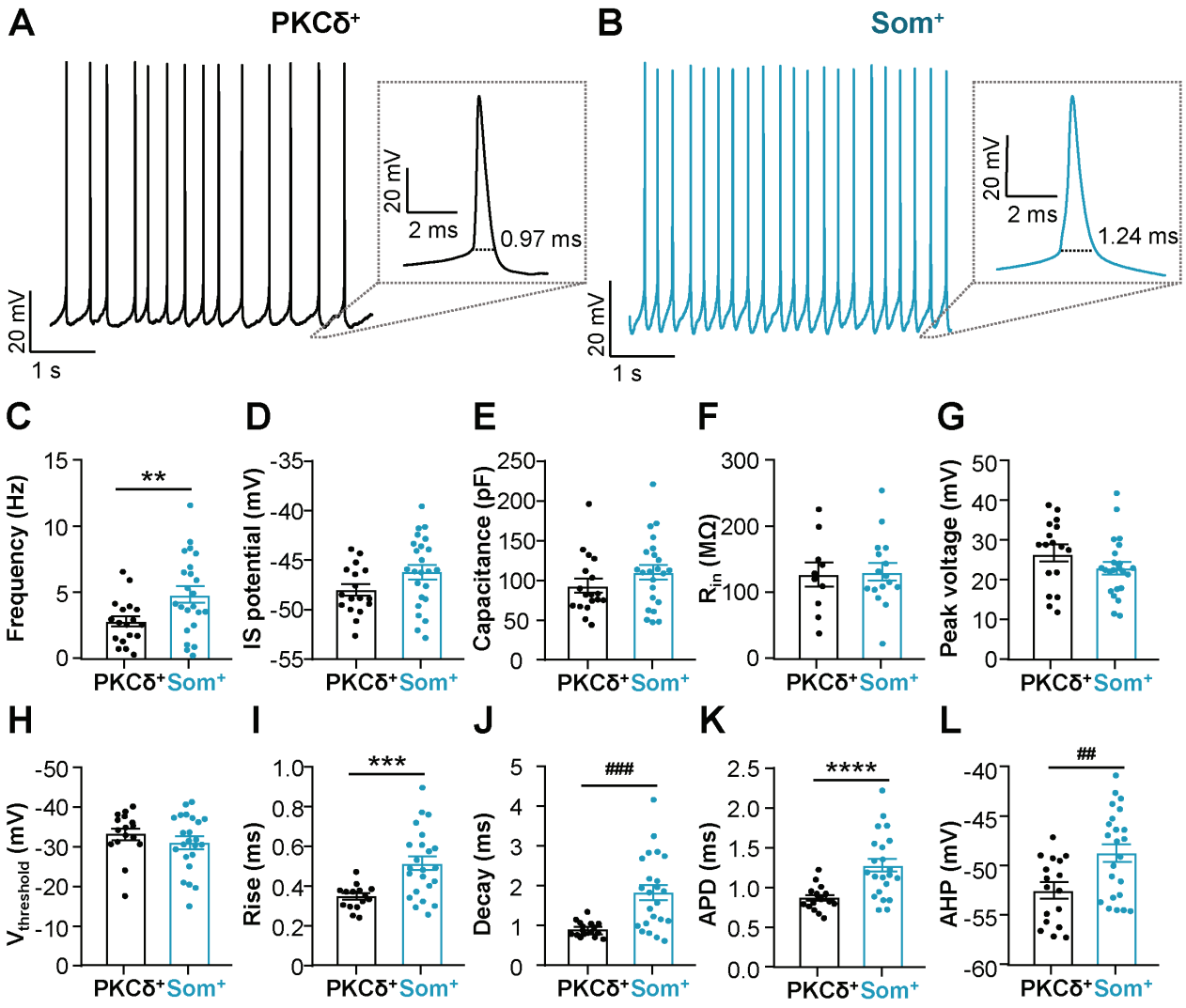

eNeuro Accepted Manuscript

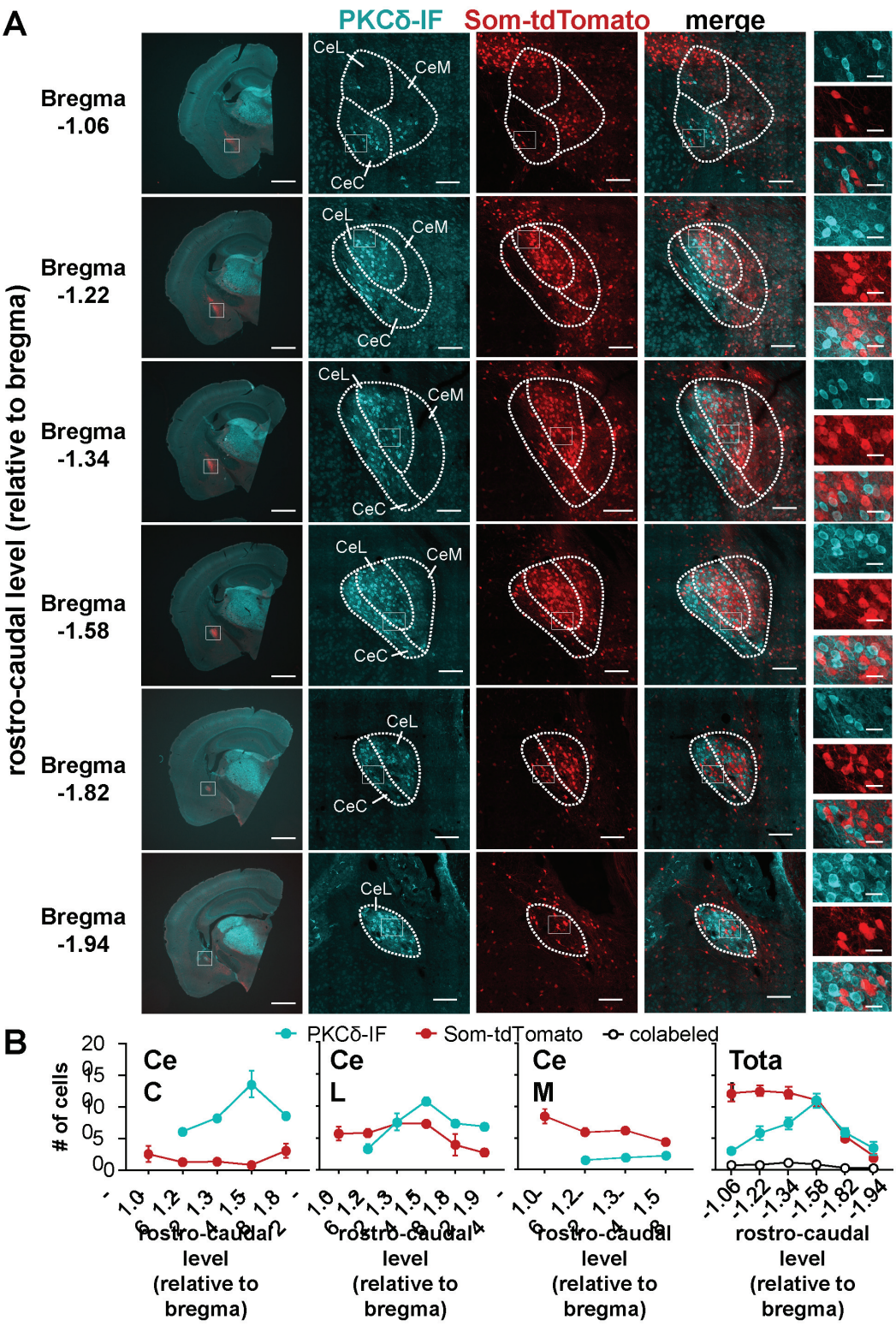

eNeuro Accepted Manuscript

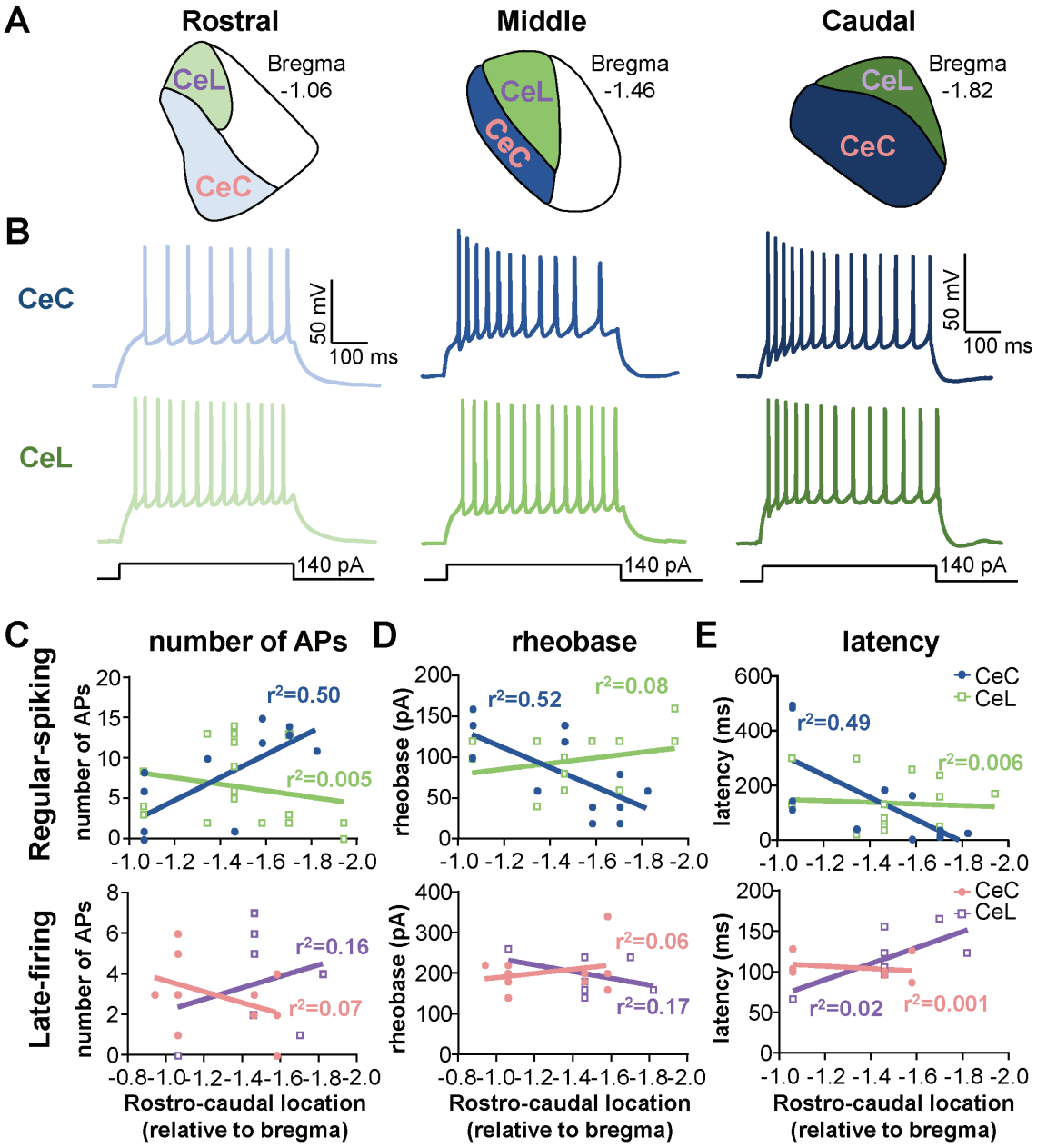

eNeuro Accepted Manuscript

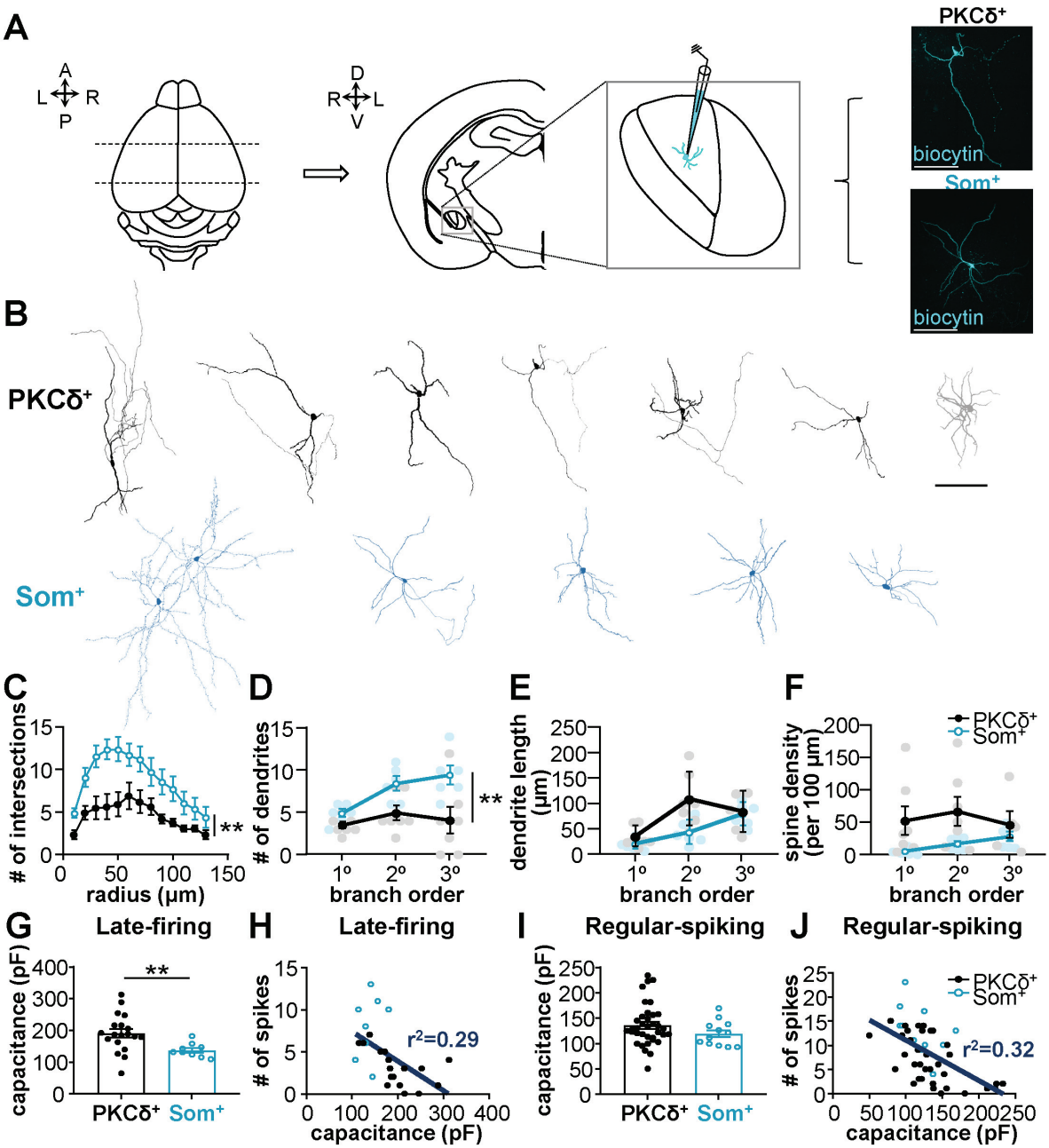

eNeuro Accepted Manuscript

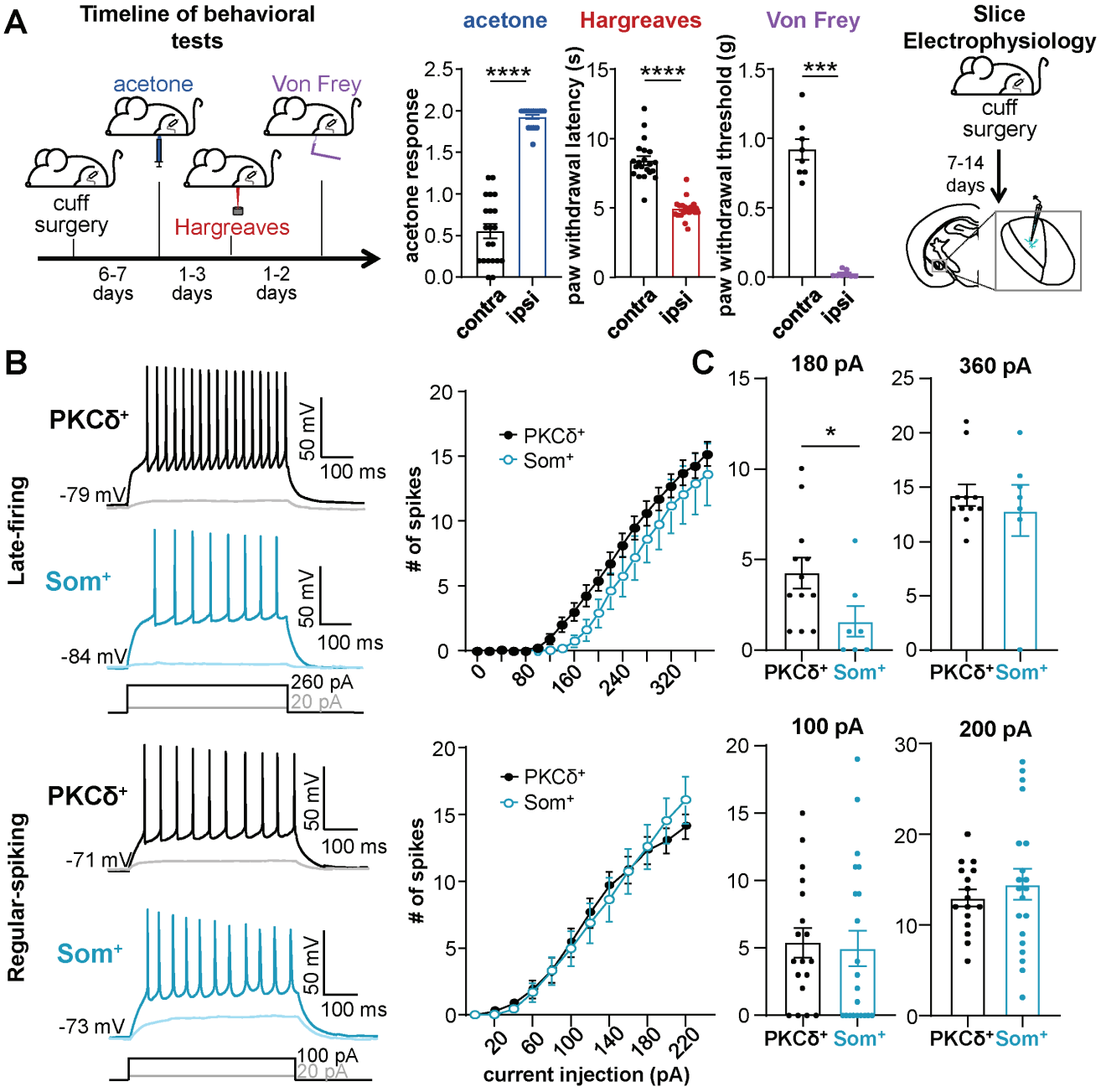

eNeuro Accepted Manuscript

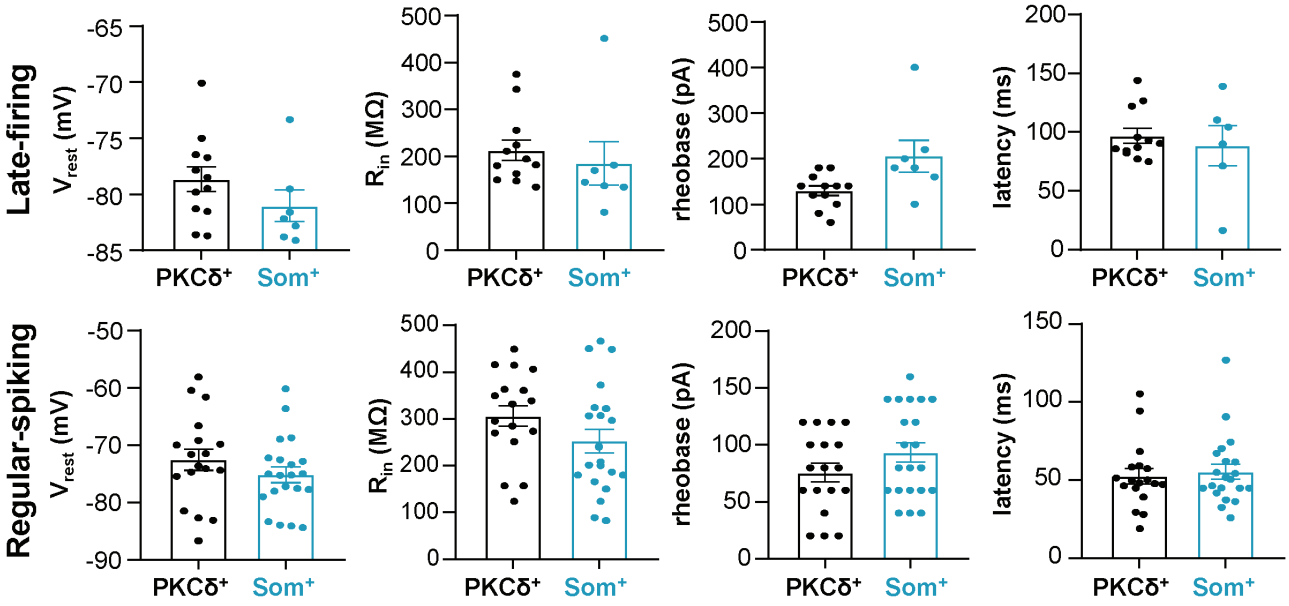

eNeuro Accepted Manuscript

	Late-firing		Regula
	Non-accommodating	**Accommodating**	**Non-accommodating**
Passive membrane properties			
V_{rest} (mV)	-78.7 ± 2.0 (n=9)	-79.5 ± 0.8 (n=8)	-77.4 ± 0.8* (n=17)
R_{in} (MΩ)	135.5 ± 23.5 (n=9)	127.3 ± 10.5 (n=8)	285.6 ± 25.6 (n=17)
Repetitive firing properties			
rheobase (pA)	204.4 ± 22.05 (n=9)	202.2 ± 9.7 (n=9)	92.9 ± 8.7 (n=17)
latency (ms)	110.5 ± 9.8 (n=8)	114.8 ± 9.3 (n=7)	69.9 ± 5.0 (n=15)
ISI accommodation	1.2 ± 0.1** (n=8)	2.0 ± 0.1** (n=7)	1.0 ± 0.06*** (n=17)
amplitude accommodation ratio	0.6 ± 0.06 (n=9)	0.7 ± 0.12 (n=7)	0.8 ± 0.01# (n=14)
width accommodation ratio	1.7 ± 0.2 (n=9)	1.7 ± 0.2 (n=7)	1.3 ± 0.04 (n=17)
AHP accommodation ratio	0.8 ± 0.02 (n=19)	0.9 ± 0.02 (n=7)	0.9 ± 0.01 (n=17)
Single action potential properties			
current threshold (pA)	1708 ± 177 (n=9)	1823 ± 108 (n=7)	808 ± 71 (n=13)
voltage threshold (mV)	-36.4 ± 2.4 (n=9)	-34.9 ± 1.9 (n=7)	-39.7 ± 1.9 (n=13)
rise (ms)	0.25 ± 0.02 (n=9)	0.26 ± 0.01 (n=7)	0.27 ± 0.01 (n=13)
decay (ms)	0.58 ± 0.02	0.57 ± 0.02	0.79 ± 0.03

eNeuro Accepted Manuscript

decay (ms)	(n=9)	(n=7)	(n=13)
width (ms)	1.09 ± 0.03 (n=9)	1.3 ± 0.02 (n=7)	1.2 ± 0.04 (n=13)
AHP (mV)	-61.0 ± 1.0 (n=9)	-59.2 ± 0.9 (n=7)	-55.0 ± 1.0 (n=13)

eNeuro Accepted Manuscript

ır-spiking	Accommodating
-70.6 ± 1.8* (n=18)	
260.6 ± 21.6 (n=18)	
76.7 ± 4.8 (n=19)	
58.4 ± 4.9 (n=15)	
1.9 ± 0.06*** (n=18)	
0.7 ± 0.03# (n=19)	
1.2 ± 0.05 (n=16)	
0.9 ± 0.01 (n=19)	
706 ± 103 (n=18)	
-41.2 ± 1.6 (n=18)	
0.29 ± 0.02 (n=18)	
0.79 ± 0.06	

(n=18)
1.5 ± 0.07 (n=18)
-57.4 ± 0.9 (n=18)

eNeuro Accepted Manuscript

eNeuro Accepted Manuscript

	Anterior (number of cells)	**Middle** (number of cells)	**Posterior** (number of cells)
CeC-PKCδ$^+$			
S	4/14	0/4	2/11
LF	5/15	2/4	3/11
RS	6/15	2/4	6/11
CeL-PKCδ$^+$			
S	2/8	5/16	3/12
LF	1/8	4/16	3/12
RS	5/8	7/16	6/12
CeC-Som$^+$			
S	1/2	0/1	1/4
LF	0/2	0/1	2/4
RS	1/2	1/1	1/4
CeL-Som$^+$			
S	7/15	5/8	3/5
LF	4/15	1/8	1/5
RS	4/15	2/8	1/5

eNeuro Accepted Manuscript

Table 3. Statistical Analyses

Figure	Data Structure	Type of Test	Sample Size	Statistical Data
Figure 1				
1D (% cell types)	parts of a whole	Chi-square	PKCδ$^+$ = 75 cells Som$^+$ = 49 cells	Chi-square = 10.42; df = 2; p = 0.0055
Figure 3				
3A (IF curve LF)	two factors (cell type and current injection)	two-way ANOVA with RM	PKCδ$^+$ LF = 19 cells Som$^+$ LF = 9 cells	cell type: $F_{(1, 25)}$ = 23.89; p < 0.0001 current injection: $F_{(1.708, 42.71)}$ = 238.4; p < 0.0001
3A(IF curve RS)	two factors (genotype and current injection)	two-way ANOVA with RM	PKCδ$^+$ RS = 36 cells Som$^+$ RS = 12 cells	cell type: $F_{(1,46)}$ = 9.440; p = 0.0036 current injection: $F_{(1.785, 82.13)}$ = 185.7; p < 0.0001
3B (latency LF)	normal distribution, same variance	unpaired t-test (two-tailed)	PKCδ$^+$ LF = 16 cells Som$^+$ LF = 9 cells	t = 3.206; df = 23; p = 0.0039; eta squared = 0.309
3C (rheobase LF)	normal distribution, same variance	unpaired t-test (two-tailed)	PKCδ$^+$ LF = 18 cells Som$^+$ LF = 9 cells	t = 2.012; df = 25; p = 0.0551; eta squared = 0.139
3D top (R_{in} LF)	non-normal distribution	Mann-Whitney U test	PKCδ$^+$ LF = 18 cells Som$^+$ LF = 9 cells	p = 0.0308 (two-tailed); U = 39
3E top (V_{rest} LF)	normal distribution, different variances	unpaired t-test with Welch's correction (two-tailed)	PKCδ$^+$ LF = 18 cells Som$^+$ LF = 9 cells	t = 4.360; df = 24.99; p = 0.0002; eta squared = 0.432
3F (latency RS)	normal distribution, same variance	unpaired t-test (two-tailed)	PKCδ$^+$ RS = 36 cells Som$^+$ RS = 12 cells	t = 1.720; df = 46; p = 0.0921; eta squared = 0.060
3G (rheobase RS)	non-normal distribution	Mann-Whitney U test	PKCδ$^+$ RS = 36 cells Som$^+$ RS = 12 cells	p = 0.2807 (two-tailed); U = 171
3H (R_{in} RS)	normal distribution, same variance	unpaired t-test (two-tailed)	PKCδ$^+$ RS = 36 cells Som$^+$ RS = 12 cells	t = 0.5057; df = 46; p = 0.6155; eta squared = 0.006
3I (V_{rest} RS)	normal distribution, same variance	unpaired t-test (two-tailed)	PKCδ$^+$ RS = 35 cells Som$^+$ RS = 12 cells	t = 0.6467; df = 45; p = 0.5211; eta squared = 0.009
Figure 4				
V_{sag} LF	normal distribution, same variance	unpaired t-test (two-tailed)	PKCδ$^+$ = 18 cells Som$^+$ = 9 cells	t = 1.723; df = 25; p = 0.0971; eta squared = 0.1062
V_{sag} RS	non-normal distribution	Mann-Whitney U test	PKCδ$^+$ = 33 cells Som$^+$ = 13 cells	p = 0.4961 (two-tailed); U = 186
Figure 5				
5Ci (PKCδ$^+$ LF peak voltage)	normal distribution	paired t-test (two-tailed)	n = 15 cells	t = 8; df = 14; p < 0.0001; eta squared = 0.8444
5Cii (Som$^+$ LF peak voltage)	normal distribution	paired t-test (two-tailed)	n = 9 cells	t = 7.088; df = 8; p < 0.0001; eta squared = 0.8626
5Ciii (accommodation ratio LF)	normal distribution, same variance	unpaired t-test (two-tailed)	PKCδ$^+$ LF = 15 cells Som$^+$ LF = 9 cells	t = 3.284; df = 22; p = 0.0034; eta squared = 0.3289
5Di (PKCδ$^+$ RS peak voltage)	normal distribution	paired t-test (two-tailed)	n = 36 cells	t = 12.24; df = 35; p < 0.0001; eta squared = 0.8107
5Dii (Som$^+$ RS peak voltage)	normal distribution	paired t-test (two-tailed)	n = 13 cells	t = 4.923; df = 12; p = 0.0004; eta squared = 0.6688
5Diii (accommodation ratio RS)	non-normal distribution	Mann-Whitney U test	PKCδ$^+$ RS = 35 cells Som$^+$ RS = 12 cells	p = 0.0687 (two-tailed); U = 135
5Ei (PKCδ$^+$ LF width)	normal distribution	paired t-test (two-tailed)	n = 14 cells	t = 4.243; df = 13; p = 0.0010; eta squared = 0.5807
5Eii (Som$^+$ LF width)	normal distribution	paired t-test (two-tailed)	n = 9 cells	t = 5.307; df = 9; p = 0.0007; eta squared = 0.7788
5Eiii (width accommodation ratio LF)	normal distribution, same variance	unpaired t-test (two-tailed)	PKCδ$^+$ LF = 16 cells Som$^+$ LF = 9 cells	t = 0.6847; df = 23; p = 0.5004; eta squared = 0.020
5Fi (PKCδ$^+$ RS width)	normal distribution	paired t-test (two-tailed)	n = 33 cells	t = 6.279; df = 32; p < 0.0001; eta squared = 0.5520
5Fii (Som$^+$ RS width)	normal distribution	paired t-test (two-tailed)	n = 13 cells	t = 6.196; df = 12; p < 0.0001; eta squared = 0.7618
5Fiii (width accommodation ratio RS)	non-normal distribution	Mann-Whitney U test	PKCδ$^+$ RS = 36 cells Som$^+$ RS = 12 cells	p = 0.0520 (two-tailed); U = 134.5
5Gi (PKCδ$^+$ LF AHP)	normal distribution	paired t-test (two-tailed)	n = 16 cells	t = 10.30; df = 15; p < 0.0001; eta squared = 0.8760
5Gii (Som$^+$ LF AHP)	normal distribution	paired t-test (two-tailed)	n = 9 cells	t = 9.170; df = 8; p < 0.0001; eta squared = 0.9131
5Giii (AHP accommodation ratio LF)	normal distribution, same variance	unpaired t-test (two-tailed)	PKCδ$^+$ LF = 16 cells Som$^+$ LF = 9 cells	t = 1.643; df = 23; p = 0.1140; eta squared = 0.105
5Hi (PKCδ$^+$ RS	normal distribution	paired t-test (two-tailed)	n = 36 cells	t = 11.03; df = 35; p < 0.0001; eta squared = 0.7766

cont. Table 3. Statistical Analyses

eNeuro Accepted Manuscript

Figure	Data Structure	Type of Test	Sample Size	Statistical Data
5Hii (Som^+ RS AHP)	normal distribution	paired t-test (two-tailed)	n = 12 cells	t = 6.368; df = 11; p < 0.0001; eta squared = 0.7866
5Hiii (AHP accommodation ratio RS)	normal distribution, different variances	unpaired t-test with Welch's correction (two-tailed)	$PKC\delta^+$ RS = 36 cells Som^+ RS = 12 cells	t = 2.821; df = 13.30; p = 0.0142; eta squared = 0.375
Figure 6				
6B ($I_{threshold}$ LF)	normal distribution, different variances	unpaired t-test with Welch's correction (two-tailed)	$PKC\delta^+$ LF = 16 cells Som^+ LF = 9 cells	t = 5.323; df = 21.33; p < 0.0001; eta squared = 0.5706
6C ($V_{threshold}$ LF)	non-normal distribution	Mann-Whitney U test	$PKC\delta^+$ LF = 16 cells Som^+ LF = 9 cells	p = 0.1687 (two-tailed); U = 47
6D (rise LF)	normal distribution, same variance	unpaired t-test (two-tailed)	$PKC\delta^+$ LF = 16 cells Som^+ LF = 9 cells	t = 0.7270; df = 23; p = 0.4746; eta squared = 0.022
6E (decay LF)	non-normal distribution	Mann-Whitney U test	$PKC\delta^+$ LF = 16 cells Som^+ LF = 9 cells	p < 0.0001 (two-tailed); U = 9
6F (width LF)	non-normal distribution	Mann-Whitney U test	$PKC\delta^+$ LF = 16 cells Som^+ LF = 9 cells	p < 0.0001 (two-tailed); U = 0
6G (AHP LF)	normal distribution, same variance	unpaired t-test (two-tailed)	$PKC\delta^+$ LF = 16 cells Som^+ LF = 9 cells	t = 2.071; df = 23; p = 0.0498; eta squared = 0.1572
6H ($I_{threshold}$ RS)	non-normal distribution	Mann-Whitney U test	$PKC\delta^+$ RS = 31 cells Som^+ RS = 10 cells	p = 0.1067 (two-tailed); U = 101.5
6I ($V_{threshold}$ RS)	normal distribution, same variance	unpaired t-test (two-tailed)	$PKC\delta^+$ RS = 31 cells Som^+ RS = 10 cells	t = 0.5674; df = 39; p = 0.5737; eta squared = 0.008
6J (rise RS)	normal distribution, same variance	unpaired t-test (two-tailed)	$PKC\delta^+$ RS = 31 cells Som^+ RS = 10 cells	t = 1.068; df = 39; p = 0.2919; eta squared = 0.028
6K (decay RS)	non-normal distribution	Mann-Whitney U test	$PKC\delta^+$ RS = 31 cells	p = 0.1720 (two-tailed); U = 109.5
6L (width RS)	normal distribution, same variance	unpaired t-test (two-tailed)	$PKC\delta^+$ RS = 31 cells Som^+ RS = 10 cells	t = 1.740; df = 39; p = 0.0898; eta squared = 0.072
6M (AHP RS)	normal distribution, same variance	unpaired t-test (two-tailed)	$PKC\delta^+$ RS = 31 cells Som^+ RS = 10 cells	t = 3.631; df = 39; p = 0.0008; eta squared = 0.2527
Figure 7				
7C (frequency)	normal distribution, different variances	unpaired t-test with Welch's correction (two-tailed)	$PKC\delta^+$ = 18 cells Som^+ = 23 cells	t = 2.790; df = 36.20; p = 0.0084; eta squared = 0.1770
7D (IS potential)	normal distribution, same variance	unpaired t-test (two-tailed)	$PKC\delta^+$ = 17 cells Som^+ = 23 cells	t = 1.88; df = 38; p = 0.077; eta squared = 0.080
7E (capacitance)	non-normal distribution	Mann-Whitney U test	$PKC\delta^+$ = 18 cells Som^+ = 23 cells	p = 0.1957 (two-tailed); U = 157
7F (R_{in})	normal distribution, same variance	unpaired t-test (two-tailed)	$PKC\delta^+$ = 10 cells Som^+ = 17 cells	t = 0.228; df = 24; p = 0.8220; eta squared = 0.002
7G (peak voltage)	normal distribution, same variance	unpaired t-test (two-tailed)	$PKC\delta^+$ = 17 cells Som^+ = 23 cells	t = 1.458; df = 38; p = 0.531; eta squared = 0.053
7H ($V_{threshold}$)	normal distribution, same variance	unpaired t-test (two-tailed)	$PKC\delta^+$ = 16 cells Som^+ = 23 cells	t = 1.020; df = 37; p = 0.315; eta squared = 0.027
7I (rise)	normal distribution, same variance	unpaired t-test (two-tailed)	$PKC\delta^+$ = 15 cells Som^+ = 23 cells	t = 3.622; df = 36; p = 0.0009; eta squared = 0.267
7J (decay)	normal distribution, different variances	unpaired t-test with Welch's correction (two-tailed)	$PKC\delta^+$ = 17 cells Som^+ = 23 cells	t = 4.604; df = 24.19; p = 0.0001; eta squared = 0.4671
7K (APD)	normal distribution, different variances	unpaired t-test with Welch's correction (two-tailed)	$PKC\delta^+$ = 17 cells Som^+ = 23 cells	t = 4.565; df = 29.88; p < 0.0001; eta squared = 0.41
7L (AHP)	normal distribution, same variance	unpaired t-test (two-tailed)	$PKC\delta^+$ = 17 cells Som^+ = 23 cells	t = 3.031; df = 38; p = 0.0044; eta squared = 0.1947

cont. Table 3. Statistical Analyses

Figure	Data Structure	Type of Test	Sample Size	Statistical Data
Figure 9				

eNeuro Accepted Manuscript

9Ci (# of APs RS)	no assumptions made about normality	linear regression	CeC:
			bregma -1.06 = 5 cells
			bregma -1.34 = 1 cell
			bregma -1.46 = 2 cells
			bregma -1.58 = 2 cells
			bregma -1.70 = 3 cells
			bregma -1.82 = 1 cell
			CeL:
			bregma -1.06 = 3 cells
			bregma -1.34 = 2 cells
			bregma -1.46 = 7 cells
			bregma -1.58 = 1 cell
			bregma -1.70 = 3 cells
			bregma -1.94 = 2 cells
				CeC:
				slope = -14.14; y-intercept = -12.20;
				x-intercept = -0.8624; r^2 = 0.5031; $F_{(1,12)}$ = 12.15;
				p = 0.0045
				CeL:
				slope = 4.001; y-intercept = 12.37;
				x-intercept = -3.091; r^2 = 0.04838; $F_{(1,16)}$ = 0.8135;
				p = 0.3805

9Cii (# of APs LF)	no assumptions made about normality	linear regression	CeC:
			bregma -0.94 = 1 cell
			bregma -1.06 = 4 cells
			bregma -1.46 = 2 cells
			bregma -1.58 = 3 cells
			CeL:
			bregma -1.06 = 1 cell
			bregma -1.46 = 4 cells
			bregma -1.70 = 1 cell
			bregma -1.82 = 1 cell
				CeC:
				slope = 2.696; y-intercept = 6.362;
				x-intercept = -2.36; r^2 = 0.1620; $F_{(1, 8)}$ = 1.546;
				p = 0.2489
				CeL:
				slope = -2.828; y-intercept = -0.6382;
				x-intercept = -0.2257; r^2 = 0.06547; $F_{(1, 5)}$ = 0.3503;
				p = 0.5797

9Di (rheobase RS)	no assumptions made about normality	linear regression	CeC:
			bregma -1.06 = 5 cells
			bregma -1.34 = 1 cell
			bregma -1.46 = 2 cells
			bregma -1.58 = 2 cells
			bregma -1.70 = 3 cells
			bregma -1.82 = 1 cell
			CeL:
			bregma -1.06 = 3 cells
			bregma -1.34 = 2 cells
			bregma -1.46 = 7 cells
			bregma -1.58 = 1 cell
			bregma -1.70 = 3 cells
			bregma -1.94 = 2 cells
				CeC:
				slope = 119.2; y-intercept = 254.3;
				x-intercept = -2.134; r^2 = 0.5193; $F_{(1, 12)}$ = 12.96;
				p = 0.0036
				CeL:
				slope = -34.19; y-intercept = 44.65;
				x-intercept = 1.306; r^2 = 0.08181; $F_{(1, 15)}$ = 1.336;
				p = 0.2657

9Dii (rheobase LF)	no assumptions made about normality	linear regression	CeC:
			bregma -0.94 = 1 cell
			bregma -1.06 = 4 cells
			bregma -1.46 = 2 cells
			bregma -1.58 = 3 cells
			CeL:
			bregma -1.06 = 1 cell
			bregma -1.46 = 4 cells
			bregma -1.70 = 1 cell
			bregma -1.82 = 1 cell
				CeC:
				slope = -50.70; y-intercept = 138.9;
				x-intercept = 2.740; r^2 = 0.063; $F_{(1, 8)}$ = 0.5384;
				p = 0.4840
				CeL:
				slope = 82.66; y-intercept = 320.2;
				x-intercept = -3.873; r^2 = 0.1674; $F_{(1, 5)}$ = 1.005;
				p = 0.3621

9Ei (latency RS)	no assumptions made about normality	linear regression	CeC:
			bregma -1.06 = 5 cells
			bregma -1.34 = 1 cell
			bregma -1.46 = 2 cells
			bregma -1.58 = 2 cells
			bregma -1.70 = 3 cells
			bregma -1.82 = 1 cell
			CeL:
			bregma -1.06 = 3 cells
			bregma -1.34 = 2 cells
			bregma -1.46 = 7 cells
			bregma -1.58 = 1 cell
			bregma -1.70 = 3 cells
			bregma-1.94 = 2 cells
				CeC:
				slope = 406.1; y-intercept = 725.4;
				x-intercept = -1.786; r^2 = 0.4858; $F_{(1, 10)}$ = 9.447;
				p = 0.0118
				CeL:
				slope = 28.59; y-intercept = 178.3;
				x-intercept = -6.235; r^2 = 0.006; $F_{(1, 14)}$ = 0.080;
				p = 0.7808

cont. Table 3. Statistical Analyses

Figure	Data Structure	Type of Test	Sample Size	Statistical Data
Figure 9				

eNeuro Accepted Manuscript

9Eii (latency LF)	no assumptions made about normality	linear regression	CeC:
			bregma -0.94 = 1 cell
			bregma -1.06 = 4 cells
			bregma -1.46 = 2 cells
			bregma -1.58 = 3 cells
			CeL:
			bregma -1.06 = 1 cell
			bregma -1.46 = 4 cells
			bregma -1.70 = 1 cell
			bregma -1.82 = 1 cell
				CeC:
				slope = -8.872; y-intercept = 208.5;
				x-intercept = 23.51; r^2 = 0.001; $F_{(1, 7)}$ = 0.010;
				p = 0.9234
				CeL:
				slope = -130.9; y-intercept = 73.09;
				x-intercept = 0.5584; r^2 = 0.026; $F_{(1, 4)}$ = 0.1087;
				p = 0.7582

Figure 10				
10C (Sholl analysis)	two factors (cell type and radial distance)	Two-way ANOVA with RM	PKCδ$^+$ = 7 cells Som$^+$ = 6 cells	cell type: $F_{(1, 11)}$ = 11.05; p = 0.0068 radial distance: $F_{(2.209, 24.30)}$ = 15.52; p < 0.0001
10D (# dendrites)	two factors (cell type and dendritic branch order)	Two-way ANOVA with RM, *posthoc* Tukey's multiple comparisons test	PKCδ$^+$ = 7 cells Som$^+$ = 6 cells	Two-way ANOVA: cell type: $F_{(1, 11)}$ = 11.85; p = 0.0055 dendritic branch order: $F_{(1.286, 14.14)}$ = 5.824; p = 0.0236 posthoc Tukey's test: PKCδ$^+$ primary v secondary dendrites: p = 0.1497 PKCδ$^+$ primary v tertiary dendrites: p = 0.9342 PKCδ$^+$ secondary v tertiary dendrites: p = 0.7940 Som$^+$ primary v secondary dendrites: p = 0.0037 Som$^+$ primary v tertiary dendrites: p = 0.0277 Som$^+$ secondary v tertiary dendrites: p = 0.7567
10E (dendrite length)	two factors (cell type and dendritic branch order)	Mixed-effects model, *posthoc* Tukey's multiple comparisons test	PKCδ$^+$ = 7 cells Som$^+$ = 6 cells	Mixed-effects: cell type: $F_{(1, 11)}$ = 4.820; p = 0.0505 dendritic branch order: $F_{(1.320, 13.20)}$ = 19.30; p = 0.0004 *posthoc* Tukey's test: PKCδ$^+$ primary v secondary dendrites: p = 0.0029 PKCδ$^+$ primary v tertiary dendrites: p = 0.0940 PKCδ$^+$ secondary v tertiary dendrites: p = 0.5862 Som$^+$ primary v secondary dendrites: p = 0.1438 Som$^+$ primary v tertiary dendrites: p = 0.0062 Som$^+$ secondary v tertiary dendrites: p = 0.0899
10F (spine density)	two factors (cell type and dendritic branch order)	Mixed-effects model, *posthoc* Tukey's multiple comparisons test	PKCδ$^+$ = 7 cells Som$^+$ = 6 cells	Mixed-effects: cell type: $F_{(1, 11)}$ = 3.730; p = 0.0796 dendritic branch order: $F_{(1.046, 10.46)}$ = 8.740; p = 0.0131 *posthoc* Tukey's test: PKCδ$^+$ primary v secondary dendrites: p = 0.0873 PKCδ$^+$ primary v tertiary dendrites: p = 0.9562 PKCδ$^+$ secondary v tertiary dendrites: p = 0.4953 Som$^+$ primary v secondary dendrites: p = 0.0227 Som$^+$ primary v tertiary dendrites: p = 0.0437 Som$^+$ secondary v tertiary dendrites: p = 0.0805
10G (capacitance LF)	normal distribution, different variances	unpaired t-test with Welch's correction (two-tailed)	PKCδ$^+$ LF = 19 cells Som$^+$ LF = 9 cells	t = 3.483; df = 25.33; p = 0.0018; eta squared = 0.3238

10H (capacitance v spikes LF)	no assumptions made about normality	linear regression	n = 27 (18 PKCδ$^+$ + 9 Som$^+$)	slope = -0.0352; y-intercept = 10.87;
				x-intercept = 308.6; r^2 = 0.2876; $F_{(1, 25)}$ = 10.09;
				p = 0.0039

10I (capacitance RS)	normal distribution, different variances	unpaired t-test with Welch's correction (two-tailed)	PKCδ$^+$ RS = 36 cells Som$^+$ RS = 13 cells	t = 1.665; df = 36.78; p = 0.1045; eta squared = 0.07006

10H (capacitance v spikes RS)	no assumptions made about normality	linear regression	n = 48 (35 PKCδ$^+$ + 13 Som$^+$)	slope = -0.0837; y-intercept = 19.47;
				x-intercept = 232.6; r^2 = 0.3189; $F_{(1, 46)}$ = 21.54;
				p < 0.0001

cont. Table 3. Statistical Analyses

Figure	Data Structure	Type of Test	Sample Size	Statistical Data
Figure 11				

eNeuro Accepted Manuscript

11Ai (acetone)	non-normal distribution	Mann-Whitney U test	ipsilateral = 21 mice contralateral = 21 mice	p < 0.0001 (two-tailed); U = 0
11Aii (Hargreaves)	non-normal distribution	Mann-Whitney U test	ipsilateral = 21 mice contralateral = 21 mice	p < 0.0001 (two-tailed); U = 2
11Aiii (von Frey)	non-normal distribution	Mann-Whitney U test	ipsilateral = 8 mice contralateral = 8 mice	p < 0.0002 (two-tailed); U = 0
11Bi (IF curve LF)	two factors (cell type and current injection)	Mixed-effects model	PKCδ$^+$ = 12 cells Som$^+$ = 7 cells	cell type: $F_{(1, 17)}$ = 1.814; p = 0.1957 current injection: $F_{(1.378, 23)}$ = 124.6; p < 0.0001
11Bii (IF curve RS)	two factors (cell type and current injection)	Mixed-effects model	PKCδ$^+$ = 18 cells Som$^+$ = 21 cells	cell type: $F_{(1, 37)}$ = 0.001; p = 0.9739 current injection: $F_{(1.549, 55.5)}$ = 144.8; p < 0.0001
11Ci (APs at 180 pA LF)	non-normal distribution	Mann-Whitney U test	PKCδ$^+$ = 12 cells Som$^+$ = 7 cells	p = 0.0314 (two-tailed); U = 17
11Cii (APs at 360 pA LF)	non-normal distribution	Mann-Whitney U test	PKCδ$^+$ = 11 cells Som$^+$ = 7 cells	p = 0.8788 (two-tailed); U = 36.50
11Ciii (APs at 100 pA RS)	non-normal distribution	Mann-Whitney U test	PKCδ$^+$ = 18 cells Som$^+$ = 21 cells	p = 0.4719 (two-tailed); U = 163.5
11Civ (APs at 200 pA RS)	normal distribution, different variances	unpaired t-test with Welch's correction (two-tailed)	PKCδ$^+$ = 16 cells Som$^+$ = 20 cells	t = 0.7728; df = 28.89; p = 0.4459; eta squared = 0.0203
Figure 12				
V_{rest} LF pain	normal distribution, same variance	unpaired t-test (two-tailed)	PKCδ$^+$ = 12 cells Som$^+$ = 7 cells	t = 1.317; df = 17; p = 0.2052; eta squared = 0.09262
V_{rest} RS pain	normal distribution, same variance	unpaired t-test (two-tailed)	PKCδ$^+$ = 18 cells Som$^+$ = 21 cells	t = 1.165; df = 37; p = 0.2515; eta squared = 0.0354
R_{in} LF pain	non-normal distribution	Mann-Whitney U test	PKCδ$^+$ = 12 cells Som$^+$ = 7 cells	p = 0.1195 (two-tailed); U = 23
R_{in} RS pain	normal distribution, same variance	unpaired t-test (two-tailed)	PKCδ$^+$ = 18 cells Som$^+$ = 21 cells	t = 1.580; df = 37; p = 0.1227; eta squared = 0.0632
rheobase LF pain	normal distribution, different variances	unpaired t-test with Welch's correction (two-tailed)	PKCδ$^+$ = 12 cells Som$^+$ = 7 cells	t = 2.050; df = 7.092; p = 0.0790; eta squared = 0.3721
rheobase RS pain	normal distribution, same variance	unpaired t-test (two-tailed)	PKCδ$^+$ = 18 cells Som$^+$ = 21 cells	t = 1.466; df = 37; p = 0.1510; eta squared = 0.0549
latency LF pain	non-normal distribution	Mann-Whitney U test	PKCδ$^+$ = 12 cells Som$^+$ = 6 cells	p = 0.9636 (two-tailed); U = 35
latency RS pain	non-normal distribution	Mann-Whitney U test	PKCδ$^+$ = 18 cells Som$^+$ = 21 cells	p = 0.8564 (two-tailed); U = 182
Table 1				
V_{rest} LF	normal distribution, different variances	unpaired t-test with Welch's correction (two-tailed)	Na = 9 cells Ac = 8 cells	t = 0.3887; df = 10.42; p = 0.7053; eta squared = 0.0143
V_{rest} RS	normal distribution, same variances	unpaired t-test (two-tailed)	Na = 17 cells Ac = 18 cells	t = 2.920; df = 33; p = 0.0063; eta squared = 0.2052
R_{in} LF	normal distribution, different variances	unpaired t-test with Welch's correction (two-tailed)	Na = 9 cells Ac = 9 cells	t = 0.3179; df = 11.09; p = 0.7565; eta squared = 0.0090

cont. Table 3. Statistical Analyses

Figure	Data Structure	Type of Test	Sample Size	Statistical Data
Table 1				

eNeuro Accepted Manuscript

R_{in} RS	normal distribution, same variances	unpaired t-test (two-tailed)	Na = 17 cells Ac = 18 cells	t = 0.7474; df = 33; p = 0.4601; eta squared = 0.0167
rheobase LF	normal distribution, different variances	unpaired t-test with Welch's correction (two-tailed)	Na = 9 cells Ac = 9 cells	t = 0.0923; df = 10.98; p = 0.9282; eta squared = 0.001
rheobase RS	non-normal distribution	unpaired t-test (two-tailed)	Na = 17 cells Ac = 19 cells	p = 0.6639 (two-tailed); U = 147.5
latency LF	normal distribution, same variances	unpaired t-test (two-tailed)	Na = 8 cells Ac = 7 cells	t = 0.3191; df = 13; p = 0.7547; eta squared = 0.008
latency RS	normal distribution, same variances	unpaired t-test (two-tailed)	Na = 15 cells Ac = 15 cells	t = 1.640; df = 28; p = 0.1122; eta squared = 0.088
ISI LF	non-normal distribution	Mann-Whitney U test	Na = 8 cells Ac = 7 cells	p = 0.0003; U = 0
ISI RS	normal distribution, same variances	unpaired t-test (two-tailed)	Na = 17 cells Ac = 18 cells	t = 10.38; df = 33; p < 0.0001; eta squared = 0.7656
amplitude accommodation LF	normal distribution, same variances	unpaired t-test (two-tailed)	Na = 9 cells Ac = 7 cells	t = 1.170; df = 14; p = 0.2616; eta squared = 0.089
amplitude accommodation RS	normal distribution, different variances	unpaired t-test with Welch's correction (two-tailed)	Na = 14 cells Ac = 20 cells	t = 4.787; df = 22.08; p < 0.0001; eta squared = 0.509
width accommodation LF	non-normal distribution	Mann-Whitney U test	Na = 9 cells Ac = 7 cells	p > 0.9999 (two-tailed); U = 31
width accommodation RS	non-normal distribution	Mann-Whitney U test	Na = 12 cells Ac = 16 cells	p = 0.3470 (two-tailed); U = 75
AHP accommodation LF	normal distribution, same variances	unpaired t-test (two-tailed)	Na = 9 cells Ac = 7 cells	t = 0.1568; df = 14; p = 0.8776; eta squared = 0.0018
AHP accommodation RS	normal distribution, same variances	unpaired t-test (two-tailed)	Na = 12 cells Ac = 16 cells	t = 1.740; df = 34; p = 0.0908; eta squared = 0.082
$I_{threshold}$ LF	normal distribution, same variances	unpaired t-test (two-tailed)	Na = 9 cells Ac = 7 cells	t = 0.5140; df = 14; p = 0.6153; eta squared = 0.0185
$I_{threshold}$ RS	non-normal distribution	Mann-Whitney U test	Na = 13 cells Ac = 18 cells	p = 0.2218 (two-tailed); U = 86
$V_{threshold}$ LF	normal distribution, same variances	unpaired t-test (two-tailed)	Na = 9 cells Ac = 7 cells	t = 0.4831; df = 14; p = 0.6365; eta squared = 0.016
$V_{threshold}$ RS	normal distribution, same variances	unpaired t-test (two-tailed)	Na = 13 cells Ac = 18 cells	t = 0.50904; df = 29; p = 0.5595; eta squared = 0.012
rise LF	normal distribution, same variance	unpaired t-test (two-tailed)	Na = 9 cells Ac = 7 cells	t = 0.5678; df = 14; p = 0.5792; eta squared = 0.023
rise RS	normal distribution, same variance	unpaired t-test (two-tailed)	Na = 13 cells Ac = 18 cells	t = 1.089; df = 29; p = 0.2851; eta squared = 0.039
decay LF	non-normal distribution	Mann-Whitney U test	Na = 9 cells Ac = 7 cells	p > 0.9999 (two-tailed); U = 31.50
decay RS	normal distribution, different variances	unpaired t-test with Welch's correction (two-tailed)	Na = 13 cells Ac = 18 cells	t = 0.007; df = 23.94; p = 0.9946; eta squared = 0
width LF	non-normal distribution	Mann-Whitney U test	Na = 9 cells Ac = 7 cells	p = 0.6065 (two-tailed); U = 26
width RS	normal distribution, different variances	unpaired t-test with Welch's correction (two-tailed)	Na = 13 cells Ac = 18 cells	t = 0.4235; df = 24.70; p = 0.6756; eta squared = 0.007
AHP LF	non-normal distribution	Mann-Whitney U test	Na = 9 cells Ac = 7 cells	t = 1.277; df = 14; p = 2225; eta squared = 0.1043
AHP RS	non-normal distribution	Mann-Whitney U test	Na = 13 cells Ac = 18 cells	p = 0.1348 (two-tailed); U = 79